

Ages of Stars and Planets in the Kepler Field Over the First Four Billion Years

2 LUKE G. BOUMA,^{1,*} LYNNE A. HILLENBRAND,¹ ANDREW W. HOWARD,¹ HOWARD ISAACSON,² KENTO MASUDA,³ AND
3 ELSA K. PALUMBO^{1,4}

4 ¹*Department of Astronomy, MC 249-17, California Institute of Technology, Pasadena, CA 91125, USA*

5 ²*Astronomy Department, University of California, Berkeley, CA 94720, USA*

6 ³*Department of Earth and Space Science, Osaka University, Osaka 560-0043, Japan*

7 ⁴*Department of Statistics & Data Science, Carnegie Mellon University, Pittsburgh, PA 15213, USA*

8 (Received 2024 June 21; Revised —; Accepted —)

ABSTRACT

Recent analyses of FGK stars in open clusters have helped clarify the precision with which a star's rotation rate and lithium content can be used as empirical indicators for its age. Here we apply this knowledge to stars observed by Kepler. Rotation periods are drawn from previous work; lithium is measured from new and archival Keck/HIRES spectra. We report rotation-based ages for 23,813 stars (harboring 795 known planets) for which our method is applicable. We find that our rotational ages (~~Deleted: accurately~~) recover the ages of stars in open clusters spanning 0.04–2.5 Gyr; they also agree with $\gtrsim 90\%$ of the independent lithium ages. The resulting yield includes 63 planets younger than 1 Gyr at 2σ , and 109 with median ages below 1 Gyr. This is about half the number expected under the classic assumption of a uniform star formation history. (~~Deleted: We find that the scarcity of sub-gigayear systems can be attributed to the star formation rate in the Kepler field dropping by a factor of 2.81 ± 0.12 over the past 3 Gyr. We observe this trend both for known planet hosts and for the parent stellar sample. This “demographic cliff” in the Galaxy’s star formation history has been previously reported, and its confirmation helps clarify the age distribution of the known transiting exoplanets.~~) (Added: The age distribution that we observe, rather than being uniform, shows that the youngest stars in the Kepler field are 3–5 times rarer than stars 3 Gyr old. This trend holds for both known planet hosts and for the parent stellar sample. We attribute the existence of this “demographic cliff” to a combination of kinematic heating and a declining star formation rate in the Galaxy’s thin disk, and highlight its impact on the age distribution of known transiting exoplanets.)

Keywords: Stellar ages (1581), Planet hosting stars (1242), Field stars (2103), Exoplanet evolution (491), Milky Way evolution (1052)

1. INTRODUCTION

Exoplanet science is thriving, fueled by the discovery of thousands of worlds orbiting close to their host stars (Borucki et al. 2010; Ricker et al. 2015). However, most known exoplanets are billions of years old. This fact leaves many gaps in our knowledge of the exact physical and dynamical origins of these objects. The reason is that processes such as thermal cooling (Fortney et al. 2007), atmospheric loss (Owen 2019), giant impacts (Raymond et al. 2014), and dynamical instabilities (Izidoro et al. 2017) are expected to be most efficient over timescales of much less than 1 Gyr. For most known exoplanets, these processes have run their course.

Corresponding author: Luke G. Bouma
bouma.luke@gmail.com

* 51 Pegasi b Fellow

Young (<1 Gyr) exoplanets represent one means of building the timeline for exoplanet evolution. Informative individual exemplars include HIP 67522 b, a Jupiter-sized planet with a sub-Neptunian mass (Rizzuto et al. 2020; Thao et al. submitted), and V1298 Tau, a resonant chain of puffy planets that is a likely precursor to the compact multiplanet systems (David et al. 2019). Population-level analyses have similarly suggested differences in the size distribution of young exoplanets relative to their older counterparts (Berger et al. 2020a; David et al. 2021; Sandoval et al. 2021; Christiansen et al. 2023; Vach et al. 2024).

Discovering a young planet requires solving two problems: finding the planet and measuring the star's age. Each problem admits a range of solutions (e.g. Marois et al. 2008; Quinn et al. 2012; Tran et al. 2024). In this article we will consider planets whose existence has been previously established using transits, and infer new stellar ages using rotation and lithium.

To begin, imagine that the ages of nearby stars in the Galaxy are uniformly distributed from 0–10 Gyr (Binney et al. 2000; Nordström et al. 2004). This approximation suggests that $\approx 1\%$ of nearby stars have $t < 100$ Myr, and $\approx 10\%$ have $t < 1$ Gyr. Studies of currently forming protoplanets (Keppler et al. 2018), and of exoplanets evolving just after disk dispersal (e.g. Klein et al. 2022), are thereby capped in their maximum achievable sample sizes by the tyranny of the galactic star formation rate.

Despite this and other observational challenges, young close-in planet discovery has matured over the past decade, primarily due to Kepler, K2, TESS, and Gaia (e.g. Meibom et al. 2013; Mann et al. 2016; Curtis et al. 2018; Livingston et al. 2018; David et al. 2019; Bouma et al. 2020; Rizzuto et al. 2020; Plavchan et al. 2020; Newton et al. 2021; Nardiello et al. 2022; Barber et al. 2022; Zhou et al. 2022; Zakhozay et al. 2022; Wood et al. 2023). The strategy pursued by most groups during the 2010s was to focus on stars with known ages—obvious members of open clusters—and to search them for transiting planets. The resulting stellar, and assumed planetary, ages are precise at the $\approx 10\%$ level. An alternative strategy, facilitated by Gaia, is to select transiting planets based on empirical youth indicators, and to then search their local neighborhoods for comoving companions (e.g. Tofflemire et al. 2021).

While stellar ensembles provide the gold standard for astronomical ages, this “cluster-first” approach has a major limitation: most stars are in the field. Only $\lesssim 1\%$ of stars within ≈ 500 pc have been associated with their birth cluster (e.g. Zari et al. 2018; Cantat-Gaudin et al. 2020; Kounkel et al. 2020; Kerr et al. 2021). The implication for known planetary ages can be appreciated by querying the NASA Exoplanet Archive (NEA; Akeson et al. 2013) for transiting planets younger than 1 Gyr. Requiring $t < 1$ Gyr at 2σ precision gives ≈ 50 such planets at the time of writing. Most of these young planets are in clusters, and were found by Kepler, K2, or TESS. However, these surveys have cumulatively discovered (**Deleted: a total of**) $\approx 5,000$ planets. Assuming a constant star formation history, we would expect an order of magnitude more sub-gigayear transiting planets (**Added: than the 50 currently known**).

This study aims to resolve two questions. First, how wrong is it to assume a uniform age distribution for transiting planet host stars? Second, where are the missing young planets? We will find that uniform is wrong by a factor of a few, and that stellar activity may be a less significant bias in young transiting planet detection than the challenge of precisely determining ages for field stars.

Despite Kepler’s main mission ending quite some time ago, the ages of many Kepler planets remain uncertain. While isochrone ages have been calculated for Kepler stars (Berger et al. 2020a) and Kepler Objects of Interest (KOIs; Petigura et al. 2022), such ages are most precise for stars whose luminosities and temperatures separate them from the main sequence. For sub-gigayear stars on the main sequence, isochrone ages are therefore limited.

Stellar rotation periods offer a promising alternative. The idea of using a star’s spin-down as a clock has a rich history (Skumanich 1972; Noyes et al. 1984; Kawaler 1989; Barnes 2003; Mamajek & Hillenbrand 2008; Angus et al. 2015). Empirical models now yield ages precise to $\lesssim 30\%$ for FGK stars between 1–4 Gyr, and constraining age posteriors for younger ages (Bouma et al. 2023). Physics-based models (Matt et al. 2015; Gallet & Bouvier 2015; Spada & Lanzafame 2020) can connect these empirical relations to the evolution of stellar winds, internal structure, and angular momentum transport.

Rotation-based ages have been reported for various subsets of Kepler stars since the early data releases (e.g. Walkowicz & Basri 2013; McQuillan et al. 2014; Reinhold & Gizon 2015; Angus et al. 2018). More recent work has further explored incorporating information from stellar kinematics (Lu et al. 2021, 2024), and from stellar colors, luminosities, and starspot amplitudes (Mathur et al. 2023). Our analysis is motivated by a few factors that can yield improvements, particularly for sub-gigayear stars. These factors are as follows.

i) The Kepler Object of Interest catalog, and our vetting of false positives within it, has now reached maturity (e.g. Thompson et al. 2018).

ii) Measured rotation periods of FGK stars in open clusters now show not only the average evolution of $P_{\text{rot}}(T_{\text{eff}}, t)$, but also how the astrophysical dispersion of stars around this average converges by the ≈ 700 Myr age of Praesepe (e.g. Curtis et al. 2019; Gillen et al. 2020; Rampalli et al. 2021; Fritzewski et al. 2021; Rebull et al. 2022; Dungee et al. 2022; Boyle & Bouma 2023).

iii) Using open cluster data, we can marginalize over the range of ages that might explain any one star’s rotation period (Bouma et al. 2023). This represents an improvement in the accuracy of uncertainty propagation relative to previous calibrations.

iv) We can identify (**Replaced: binary stars replaced with: stars that are binaries and that have high metallicity**) with greater fidelity (**Deleted: than in the past**), which can clarify otherwise problematic estimates of rotation-based ages.

v) New open clusters in various stages of dissolution have been found in the Kepler field (e.g. Kounkel & Covey 2019; Kerr et al. 2021; Barber et al. 2022). These clusters offer stars that we can use to test the reliability of (**Replaced: the available single-star replaced with: our**) age-dating methods.

Recent years have also yielded improvements in the lithium age scale. Lithium ages include depletion boundary ages for M dwarfs and brown dwarfs in star clusters, and decline-based ages for individual field FGK stars (Soderblom 2010). The latter approach relies on the observed decrease of Li abundances in partially-convective stars as they age (e.g. Sestito & Randich 2005). The theoretical explanation for these observations is debated (e.g. Chaboyer et al. 1995; Denissenkov et al. 2010; Carlos et al. 2019). Empirical understanding however has improved due to work by Jeffries

¹⁷¹ et al. (2023), who modeled the time evolution of the Li I
¹⁷² 6708 Å equivalent width (EW) using a set of 6,200 stars in 52
¹⁷³ open clusters. Two-sided lithium ages are useful for Kepler
¹⁷⁴ (FGK) stars between \approx 0.03-0.5 Gyr, though with a strong de-
¹⁷⁵ pendence on spectral type. The precision of lithium ages in
¹⁷⁶ this regime are now in the range of 0.3-0.5 dex.

¹⁷⁷ We discuss our method for selecting the star and planet
¹⁷⁸ samples in Section 2, and describe the origin of our adopted
¹⁷⁹ stellar parameters other than ages in Section 3. We present
¹⁸⁰ our age-dating methods in Sections 4 and 5, and test them
¹⁸¹ in Section 6 using clusters in the Kepler field. We discuss
¹⁸² population-level trends in Sections 7 and 8, and offer a few
¹⁸³ conclusions in Section 9.

184 2. SELECTING THE STARS AND PLANETS

¹⁸⁵ This work is focused on Kepler stars for which ages can
¹⁸⁶ be inferred using either rotation, lithium, or both. Such
¹⁸⁷ stars are a minority of the \approx 160,000 Kepler targets. Rotational
¹⁸⁸ periods have been reported for roughly one in three Kepler
¹⁸⁹ targets (e.g. McQuillan et al. 2014; Santos et al. 2021).
¹⁹⁰ High-resolution spectra suitable for measurement of the Li I
¹⁹¹ 6708 Å doublet have only been acquired for the Kepler ob-
¹⁹² jects of interest (KOIs), which comprise a few percent of
¹⁹³ Kepler's targets. In the following, we will describe the set
¹⁹⁴ of stars that we adopt with measured rotation periods (Sec-
¹⁹⁵ tion 2.1), the set of objects we adopt as hosting planets (Sec-
¹⁹⁶ tion 2.2), and the subset of these with high-resolution spectra
¹⁹⁷ suitable for lithium analysis (Section 2.3). Figure 1 provides
¹⁹⁸ a visualization of the various samples.

199 2.1. Stellar Rotation Periods

²⁰⁰ To select stars with rotation periods, we turn to previous
²⁰¹ work. Many investigators have derived rotation periods both
²⁰² specifically for KOIs (McQuillan et al. 2013; Walkowicz &
²⁰³ Basri 2013; Mazeh et al. 2015; Angus et al. 2018; David et al.
²⁰⁴ 2021), and also for the broader set of all Kepler target stars
²⁰⁵ (McQuillan et al. 2014; Reinhold & Gizon 2015; Santos et al.
²⁰⁶ 2019, 2021; Reinhold et al. 2023). These studies used a range
²⁰⁷ of detection methods and selection functions. We are inter-
²⁰⁸ ested in understanding the age distribution of all Kepler tar-
²⁰⁹ get stars irrespective of KOI status. Out of these studies, the
²¹⁰ most homogeneous (**Deleted: and precise**) analyses of both
²¹¹ Kepler targets and KOIs appear to be those by Santos et al.
²¹² (2019, 2021), hereafter S19 and S21. For a discussion of the
²¹³ work by Reinhold et al. (2023), please see Appendix A. S19
²¹⁴ and S21 combined a wavelet analysis and autocorrelation-
²¹⁵ based approach, and cumulatively reported rotation periods
²¹⁶ for 55,232 main-sequence and subgiant FGKM stars. They
²¹⁷ included known KOIs and binaries in their analysis, and re-
²¹⁸ moved transits and eclipses during the stellar rotation mea-
²¹⁹ surement process.

²²⁰ We therefore adopt the results of S19 and S21 as our de-
²²¹ fault rotation periods. S21 provided a comparison against
²²² McQuillan et al. (2014) (hereafter M14); the brief summary
²²³ is that the periods agree for 99.0% of the 31,038 period de-
²²⁴ tections in common between the two studies. S21 classified
²²⁵ the 2,992 remaining stars from M14 as not showing rotation

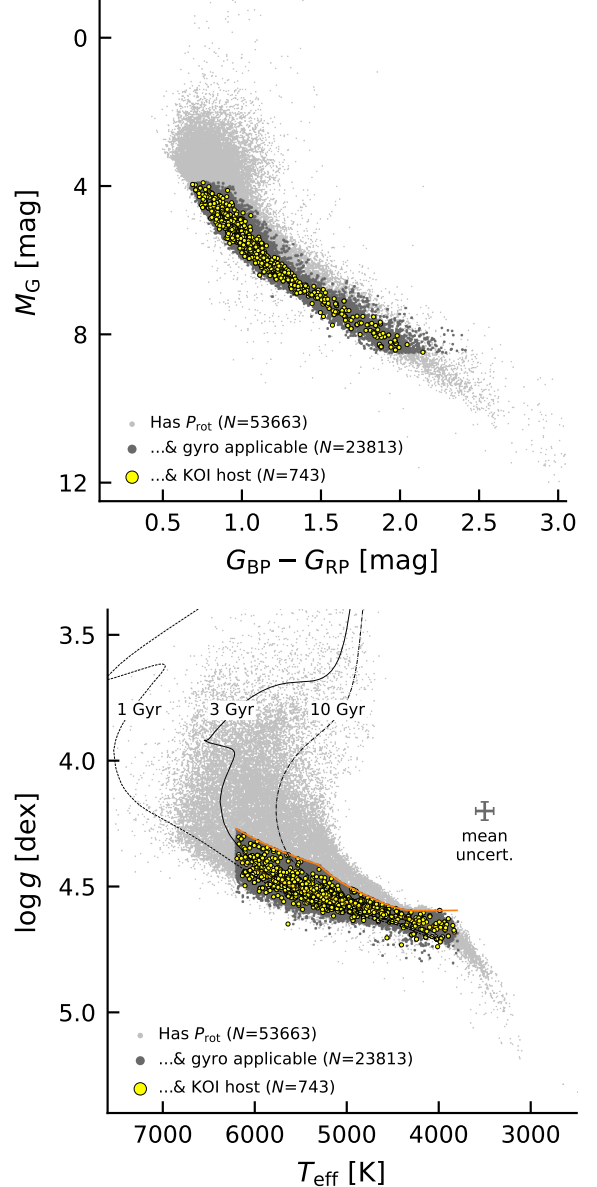


Figure 1. The stars. Our analysis focuses on stars observed by Kepler with previously reported rotation periods (gray points). The rotation periods are primarily drawn from Santos et al. (2019, 2021). About half of the stars with rotation periods are suitable for gyrochronology (dark gray points), based on factors including their non-binarity and proximity to the main sequence (orange line in lower panel; see Section 4.1). Some host “confirmed” or “candidate” KOIs that meet additional planetary quality criteria (yellow points; Section 4.2). Surface gravities and effective temperatures were derived photometrically by Berger et al. (2020b). Isochrones in the lower panel are from MIST (Choi et al. 2016).

²²⁶ periods based on updated knowledge of contaminants (such
²²⁷ as giant stars and eclipsing binaries) and visual inspection.
²²⁸ In addition, S21 reported rotation periods for 24,182 main-
²²⁹ sequence and subgiant FGKM stars that were not reported as

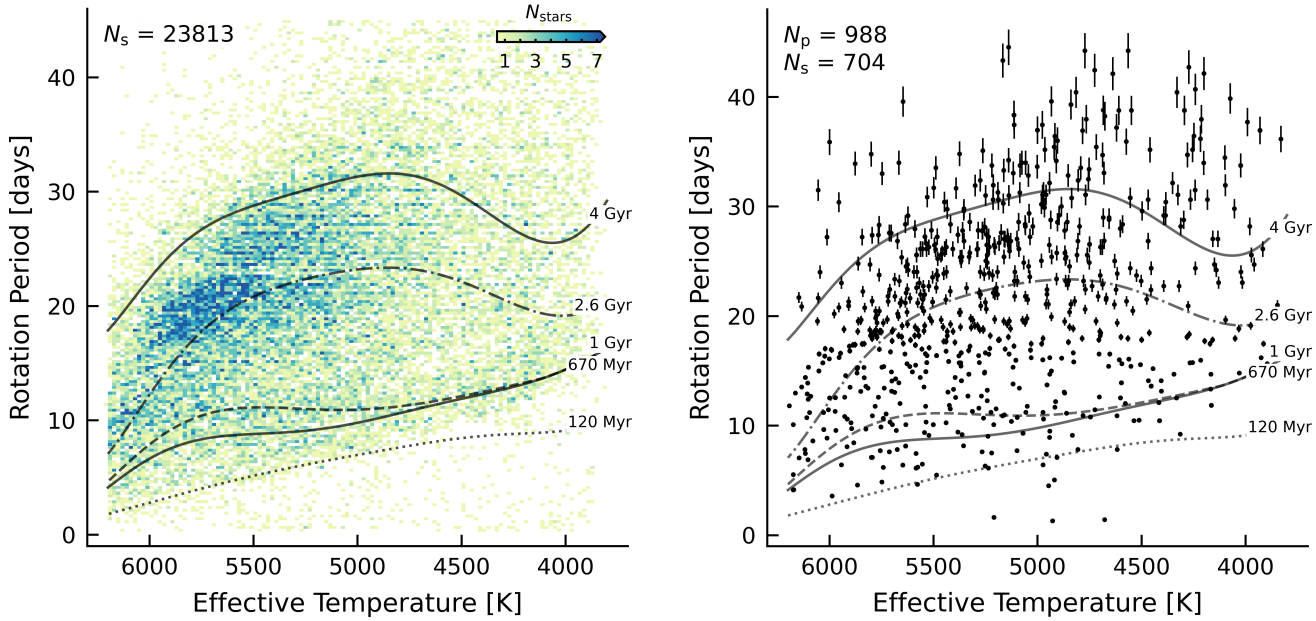


Figure 2. Rotation periods for Kepler target stars (left) and known planet hosts (right). The gray lines are (Replaced: “mean fits” to the rotation sequences of open clusters replaced with: seventh-order polynomials fitted to the slow rotation sequences of open clusters (see Section 3.3 of Bouma et al. 2023)). The 2-D histogram of the stellar sample (left) includes only apparently single stars near the main sequence with $\log g > 4.2$, $\text{RUWE} < 1.4$, and temperatures of 3800–6200 K. The planet hosts (right) require the same stellar cuts, and include only the confirmed and candidate planets described in Section 4.2. The number of stars N_s and planets N_p are noted in the relevant panels. A simple estimate for the number of young planets discovered by Kepler follows by counting points below the (Deleted: mean-) rotational isochrones.

periodic by M14. Many of these reported signals have lower variability amplitudes and longer periods than those reported by M14.

Analyzing the compilation of S19 and S21 rotation periods for the KOI hosts, we noticed that some known KOIs with rotation periods were missing. This is not surprising, since the rotation periods of KOIs have received more scrutiny than those of ordinary Kepler stars. We therefore decided to split our subsequent analysis into a homogeneous portion that used only the S19 and S21 data, and an inhomogeneous portion that also considered a broader set of available KOI rotation periods. For the latter portion, we first included 32 KOIs with orbital and rotation periods within $\approx 20\%$ that had been excluded from the S19 and S21 catalogs (A. Santos, private communication). We then incorporated an additional 178 rotation periods for KOI hosts that David et al. (2021) described as either “reliable” or “highly reliable” in their visual analysis of previously reported KOI rotation periods from McQuillan et al. (2013), Walkowicz & Basri (2013), Mazeh et al. (2015) and Angus et al. (2018). Inclusion of these additional KOI rotation periods is a supplementary measure aimed at completeness in our final KOI age catalog; the provenances of the individual adopted periods are noted in the relevant tables.

Finally, since our scope is focused on rotation-based ages, we restricted our attention to stars with reported $P_{\text{rot}} < 45$ days. The slowest-rotating FGK stars in the open clusters used to calibrate our gyrochronology model have $P_{\text{rot}} \approx 35$ days. Figure 2 shows a subset of the resulting

53,663 Kepler stars with rotation periods compiled from S19, S21, and our extended KOI list.(Added: The gray lines in this figure are the polynomials described by Bouma et al. (2023) that fit the slow rotation sequences of the Pleiades (Rebull et al. 2016), Praesepe (Rampalli et al. 2021), NGC-6811 (Curtis et al. 2019), NGC-6819 (Meibom et al. 2015), Ruprecht-147 (Curtis et al. 2020), and M67 (Barnes et al. 2016; Dungee et al. 2022; Gruner et al. 2023).)

To assess the statistical uncertainties of (Replaced: these replaced with: our adopted) rotation periods, we compared our (Deleted: adopted) periods with those reported by McQuillan et al. (2014). The details are in Appendix A. We found that for $P_{\text{rot}} \lesssim 15$ days, the two datasets agree at a precision of $\lesssim 0.01 P_{\text{rot}}$. At longer periods of $P_{\text{rot}} \approx 30$ days, the agreement was typically at the $\lesssim 0.03 P_{\text{rot}}$ level, and the envelope of the period difference increased roughly linearly with period. Based on this comparison, we adopted a simple prescription for the period uncertainties, such that there are 1% relative uncertainties below $P_{\text{rot}} = 15$ days, and a linear increase thereafter, with slope set to require 3% P_{rot} uncertainties at rotation periods of 30 days.

2.2. Kepler Objects of Interest

We considered planets in the NEA cumulative KOI table as of 2023 June 6, which included the best knowledge available on any given planet candidate while also incorporating human-based vetting. These planets represent a super-

set of those in the fully automated Q1–Q17 DR25 KOI Table (Thompson et al. 2018), which could be adopted in future work for planet occurrence rate calculations. This version of the cumulative KOI table included 4,716 objects that are either “confirmed” or “candidate” planets, after excluding known false positives.

2.3. High Resolution Spectra

The final piece of our analysis involves assessing ages based on the Li I 6708 Å doublet. We analyzed spectra from the High Resolution Echelle Spectrometer (HIRES; Vogt et al. 1994a) on the Keck I 10m telescope. These spectra were primarily collected through the California Kepler Survey (Petigura et al. 2017; Johnson et al. 2017; Fulton et al. 2017). We supplemented the existing archive with ≈ 10 hours of new observations for 22 stars between Fall 2022 and Spring 2024. These stars were chosen to ensure that confirmed planets with rotational evidence for ages below 1 Gyr had spectra, since this is the age range in which lithium is most likely to yield useful age constraints.

Lithium equivalent widths and abundances for the Kepler Objects of Interest were already analyzed by Berger et al. (2018) for roughly three quarters of the spectra in our sample. However, new spectra have since been acquired, and our approach and selection function are different. We therefore performed our own line width measurements on the reduced HIRES spectra.

We collected all blaze-corrected HIRES spectra from our group’s observations of non-false positive Kepler Objects of Interest with a “multiple event statistic” (MES, `koi_max_mult_ev`) of at least 10. This yielded at least one spectrum for 1,464 stars hosting 2,174 planets. About half of these stars have measured rotation periods (797 stars and 1,170 planets, respectively). For stars with multiple spectra available, we analyzed only the spectrum with the highest number of counts. The resulting spectra were acquired between 2009 September 6 and 2024 May 16, and cumulatively comprise 304 hours of open-shutter time.

We measured the lithium equivalent widths using a procedure adapted from previous work (Bouma et al. 2021). Our stars of interest are FGK stars, and so the continuum in the vicinity of the Li I 6708 Å doublet is well-defined. We Doppler-corrected the spectra to a common reference wavelength by cross-correlating against a high S/N template for Kepler-1698, chosen because $|\gamma| < 10 \text{ km s}^{-1}$, $T_{\text{eff}} \approx 5000 \text{ K}$ and $v \sin i \approx 5 \text{ km s}^{-1}$, which puts it in the middle of our sample’s temperature range and gives it mild line-broadening. We then trimmed the Doppler-corrected spectra to a local window centered on the lithium line, using a window width of 15 Å (we also considered 10 Å and 20 Å; the results were consistent). We continuum-normalized by fitting a third-degree Chebyshev series, while excluding regions with absorption lines. We then numerically integrated the resulting spectrum using a one-component Gaussian with free amplitude, width, and mean, and estimated uncertainties on the line width through a Monte Carlo procedure that bootstrapped

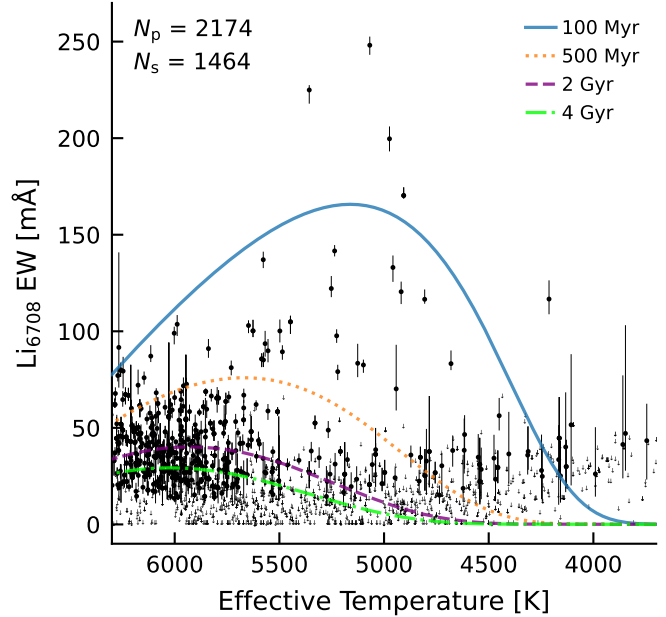


Figure 3. Equivalent widths (EW) of the Li I 6708 Å doublet for planet-hosting stars. These measurements were made from Keck/HIRES spectra collected from 2009–2024. Lines are the “mean” isochrones from Jeffries et al. (2023). The intrinsic dispersion around these isochrones becomes much larger than changes in the mean at $\gtrsim 1$ Gyr (see Figure 4). Some stars with lithium detections do not have detected rotation periods, and vice-versa.

against the local scatter in the continuum. The resulting EWs are shown in Figure 3.

Our EW measurement approach did not correct for the neighboring Fe I 6707.44 Å blend. To evaluate the accuracy and precision of our method, after applying an initial iteration on the 1,464 stars with spectra, we compared our lithium equivalent widths with those reported by Berger et al. (2018). For the stars in both samples, we found broad agreement at $> 30 \text{ m}\AA$, and significant differences at $< 30 \text{ m}\AA$ because Berger et al. (2018) required positive EWs, while we allowed for statistically negative ones. At $> 30 \text{ m}\AA$, there is however a small offset in our respective scales caused by our non-treatment of the iron blend, such that $(B24 - B18) = 7.50 \pm 8.55 \text{ m}\AA$. We therefore directly subtracted this constant mean value ($7.50 \text{ m}\AA$) when calculating lithium-based ages. This offset is at worst five times smaller than the astrophysical scatter present in lithium EWs for calibration clusters at any given age (see Jeffries et al. 2023).

3. STELLAR PROPERTIES

Our default source for stellar temperatures and surface gravities was the Gaia-Kepler Stellar Properties Catalog (GKSP; Berger et al. 2020b). The GKSP parameters were reported for stars with “AAA” 2MASS photometry, measured parallaxes in Gaia DR2, and *g*-band photometry available from either SDSS or else Kepler-INT (Greiss et al. 2012). The parameters themselves were derived using

isoclassify (Huber et al. 2017) to interpolate over the MIST isochrone grids (Choi et al. 2016; Dotter 2016), given the SDSS g and 2MASS K_s photometry, the Gaia DR2 parallaxes, and V -band extinction from the Green et al. (2019) reddening map. The resulting stellar parameters are available for $\approx 94\%$ of the 53,663 Kepler stars with rotation periods. For the remaining $\approx 6\%$ of stars that lack temperatures and surface gravities from B20, we adopted the values reported by Santos et al. (2019) and Santos et al. (2021), which are primarily derived from the photometric Mathur et al. (2017) DR25 Kepler Stellar Properties Catalog. In the planet sample, $\approx 92\%$ of the non-false-positive KOIs with rotation periods have parameters from Berger et al. (2020b), and the remainder are drawn from DR25.

David et al. (2021) compared the photometric B20 stellar parameters (T_{eff} , R_* , [Fe/H]) against the spectroscopic parameters from Fulton & Petigura (2018). The temperature scales showed a few-percent systematic difference, with F18 quoting higher temperatures than B20 for mid K dwarfs, and lower temperatures for early F dwarfs. Our age analysis, described below, adopts the maximum of the two-sided uncertainties reported by B20 as a symmetric Gaussian temperature uncertainty. Systematic uncertainties in the temperature scale generally influence our age uncertainties at a smaller level than the statistical intrinsic scatter in the open cluster rotation sequences.

4. AGES FROM ROTATION

We calculated gyrochrone ages using `gyro-interp` ((Added: v0 . 6;) Bouma et al. 2023), which is a method designed to address the fact that stars with the same mass and same rotation period can have a wide range of ages (e.g. Gallet & Bouvier 2015). The gyrochrone age posterior should therefore incorporate the intrinsic population-level scatter into its statistical precision. Figure 4 highlights this problem, particularly in regions where the 0.1–1 Gyr stars overlap.

To estimate the stellar spin-down rate as a function of time and stellar temperature, `gyro-interp` uses measured rotation periods and effective temperatures from reference open clusters, and interpolates between them using cubic Hermite polynomials. We calculated the probability of the rotation-based age, t_{gyro} , given the observed periods and temperatures (and their uncertainties) by integrating Equation 1 of Bouma et al. (2023). This procedure marginalizes over the astrophysical scatter that is observed in the open cluster sequences. We adopted a linear age grid spanning 0–5 Gyr with 500 grid points, and interpolated the resulting posteriors to calculate any summary statistics. The oldest cluster for which `gyro-interp` is calibrated(Added: in v0 . 6) is the 4 Gyr M67 cluster (Dungee et al. 2022; Gruner et al. 2023). For (Deleted: Kepler-)stars with rotation periods above the M67 sequence, our resulting age constraints are(Added: therefore) quoted as lower limits.

(Added: Finally, we opted to modify `gyro-interp` in v0 . 6 to incorporate an age-dependent population-level Gaussian scatter, as detailed in the change log

at [gyro-interp.readthedocs.io](#). While age precisions at ≤ 1 Gyr are unaffected, this update accounts for the observed intrinsic scatter in Ruprecht-147 and M67 being larger than in Praesepe or NGC-6811, potentially due to differential rotation (e.g., Epstein & Pinsonneault 2014). For ≈ 2 –4 Gyr old stars with rotation periods measured at $\approx 5\%$ precision, this change yields a $\lesssim 50\%$ increase in age uncertainties.)

4.1. Stellar Quality Flags

We calculated gyrochrone ages for all 45,229 stars with reported rotation periods that had effective temperatures of 3800–6200 K. To identify stars for which we suspect these ages may not be valid, we then built a set of quality flags which we condensed into a single binary number: Q_{star} . When and how this bitmask should be applied depends on the question being asked. If the goal is to construct a false-positive free sample, all the quality flags could be applied. If the goal is to construct a complete sample, then consider the examples of Kepler 1627Ab (≈ 40 Myr) and Kepler 51c (≈ 625 Myr). The former has a high RUWE due to a resolved binary companion (Bouma et al. 2022a); the latter is on a grazing orbit (Masuda 2014). We leave selection for or against such cases as a decision to the user. For our own analysis, we assume that a star is suitable for gyrochronology if none of bits zero through (Replaced: nine replaced with: ten) (inclusive) are raised. For analyses that require all stellar rotation periods to come from the same detection pipeline, we further require bit (Replaced: 11 replaced with: 12) to be zero.

Three assumptions must hold for a rotation-based age dating method like `gyro-interp` to be valid. 1) The evolutionary state of the star must be well-specified by its temperature and its age, 2) the star’s spin-down must not be influenced by binary companions, and 3) the rotation period distribution for field stars of a given temperature and age must be identical to that of equally aged open clusters (metallicity differences, for instance, are ignored). A rephrasing of the first condition is that the star must be “near the main sequence” because during the post main sequence stellar temperatures change. From ≈ 0.08 to ≈ 3 Gyr, the stars of interest in this work (3800–6200 K, 0.5 – $1.2 M_{\odot}$) have temperatures constant to $\approx 1\%$ (Choi et al. 2016). From ≈ 3 –4 Gyr, a $1.2 M_{\odot}$ star’s temperature drops from ≈ 6200 K to ≈ 6000 K ($\approx 3\%$), because its outer layers expand as it begins hydrogen shell burning as a subgiant. We treat this issue in a manner discussed in “bit 9” below.

Temperature range (bit 0)—We require stars to have effective temperatures T_{eff} between 3800 and 6200 K in order to report gyrochrone ages (Bouma et al. 2023). Stars hotter than 6200 K spin down very slowly, if at all. Stars cooler than 3800 K do spin down over gigayear timescales (Newton et al. 2016; Engle & Guinan 2023; Chiti et al. 2024), but the currently available open cluster data have yet to clarify when the intrinsic scatter in the population decreases.

Surface gravity (bit 1)—We flagged stars as possible subgiants if they had $\log g < 4.2$.

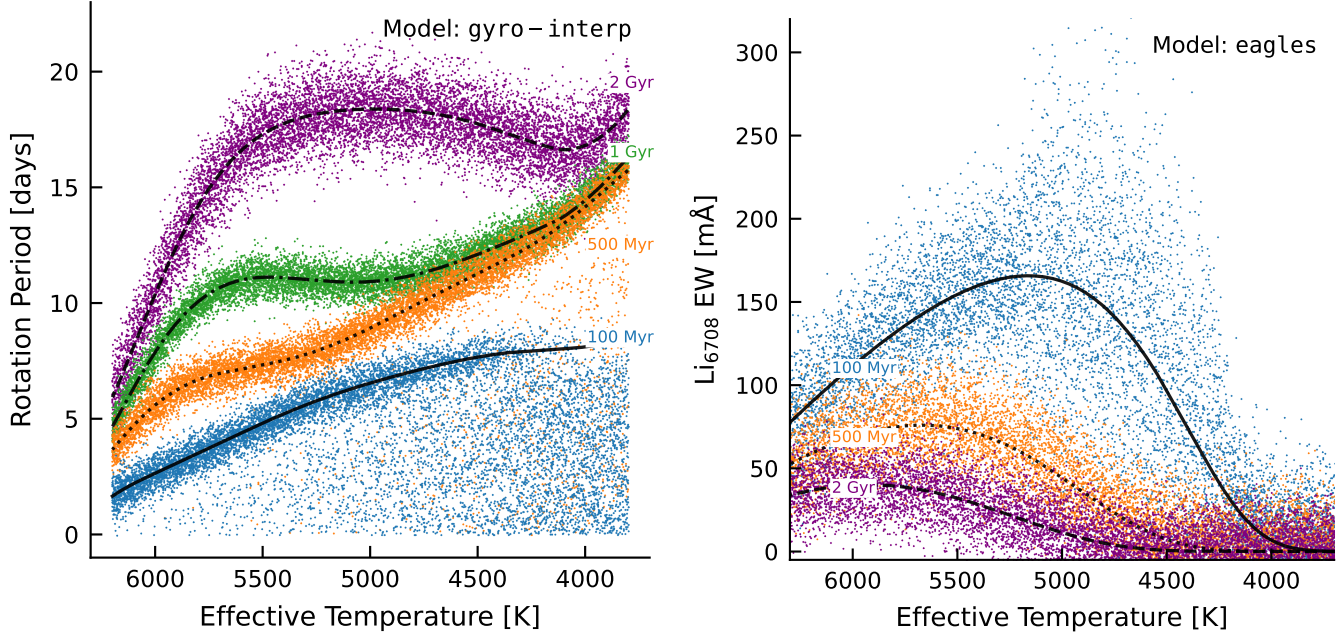


Figure 4. The models. Points represent 10^4 draws from models that have been fitted to rotation periods (Bouma et al. 2023) and lithium equivalent widths (EWs; Jeffries et al. 2023) of stars in open clusters. Lines are the “mean models” at various ages. The intrinsic dispersion around the mean, which is what the models fit, sets the theoretical precision floor for the age-dating methods. Additional sources of uncertainty, including measurement uncertainty, impose further limits on achievable precision. These models are calibrated using data from open clusters. The sizes of the points are the same in each panel, so that low apparent density signifies greater dispersion around the mean.

Absolute luminosity (bit 2)—We calculated the absolute Gaia DR3 G -band luminosity, ignoring reddening, using the reported apparent G -band magnitude and parallaxes. We flagged stars with $M_G < 3.9$ or $M_G > 8.5$, corresponding to main-sequence spectral types earlier than \approx F8V or later than \approx M0.5V (Pecaut & Mamajek 2013).

Known eclipsing binaries (bit 3)—We flagged any stars reported to be in the final Kepler eclipsing binary catalog (KEBC; Kirk et al. 2016).

Kepler-Gaia crossmatch quality (bits 4 and 5)—To leverage Gaia DR3 data, we used M. Bedell’s 4'' Kepler-to-Gaia crossmatch of the NEA q1_q17_dr25_stellar catalog with Gaia DR3 (available at <https://gaia-kepler.fun>). The separation distribution of the Kepler-Gaia DR3 crossmatches is such that 99.2% of candidate matches are within 1''. We nonetheless noted an upturn in the candidate match rate from 3-4''; such sources are flagged using bit 4. For KIC stars with multiple potential Gaia matches within the 4'' radius, we adopted the brightest star as the default match. In most such cases this was unambiguous because there is a large brightness difference between the primary and any apparent neighbors. However cases with multiple stars within 4'' within $\Delta G < 0.5$ mag are noted using bit flag 5.

Gaia DR3 non-single-stars (bit 6)—The Gaia DR3 non_single_star column in the gaia_source table flags known eclipsing, astrometric, and spectroscopic binaries. We directly included this column.

RUWE (bit 7)—We inspected diagrams of the Gaia DR3 renormalized unit weight error (RUWE) as a function of

other stellar parameters, and flagged stars with $\text{RUWE} > 1.4$ as possible binaries. Such astrometric outliers can be either bona fide astrometric binaries, or more often are marginally resolved point sources for which a single-source PSF model provides a poor fit.

Crowding (bit 8)—We searched the Gaia DR3 point source catalog for stars within 1 Kepler pixel (4'') of every target star. While such companions may not be physically associated with the target star, their presence can confuse rotation period measurements. We therefore flagged any stars with neighbors down to 1/10th the brightness of the target star within this region ($\Delta G < 2.5$). (Added: We also considered a deeper cut ($\Delta G < 5$), and found it had negligible impact on our conclusions.)

Near the main sequence (bit 9)—Figure 1 shows that many stars observed by Kepler are far from the main sequence. Some of the challenges this introduces for rotation-based ages include unresolved binaries, metallicity, reddening, and drivers of rotation other than magnetic braking. After exploring various options, we settled on the orange locus in the $\log g - T_{\text{eff}}$ plane shown in Figure 1 as a way of flagging unresolved binaries, as well as evolved late-F and early-G stars. While the exact details of how this locus is constructed are arbitrary (see Appendix B), the general aim is to flag stars for which there is evidence based on their location in the (Replaced: HR replaced with: HR or Kiel) diagram (Added: s) that our gyrochronology model may not be reliable. While the $\log g - T_{\text{eff}}$ cut flags about half of Kepler stars with rotation periods as potentially not being suit-

able for gyrochronology, a few outliers in M_G vs. $G_{\text{BP}}-G_{\text{RP}}$ remained after applying it. Such outliers are likely also questionable. We therefore also fitted a polynomial to the KOI main sequence in M_G vs. $G_{\text{BP}}-G_{\text{RP}}$, and flagged stars more than 1 magnitude from this locus as part of the same bitflag.

(Added: Metallicity (bit 10)—Theoretical models suggest that stars with non-solar metallicities spin down at different rates than solar-metallicity stars (Amard & Matt 2020). This expectation has been hard to verify due to a dearth of nearby non-solar metallicity open clusters. However, if true, this effect could cause systematic biases for gyrochronology ages (e.g. Figure 9 of Claytor et al. 2020). We therefore flagged stars with spectroscopic $|[\text{Fe}/\text{H}]| > 0.3$ from either LAMOST DR5 (Zong et al. 2018) or CKS (Petigura et al. 2022) as being outside the range of our gyrochronology calibration. We discuss limitations of this approach in Section 8.)

Candidate pulsators and close-in binaries (bit (Replaced: 10 replaced with: 11))—Santos et al. included in a flag for candidate “classical pulsators” (e.g. Cepheids) and close-in binaries. Visual inspection shows that although this flag selects many bona fide objects in these classes, it also selects most known young planets with $P_{\text{rot}} \lesssim 5$ day. These objects are neither classical pulsators nor close binaries. While we propagated this flag into our set of quality flags, we therefore generally ignore it.

Not in the homogeneous stellar rotation sample (bit (Replaced: 11 replaced with: 12))—This flag was set for the KOIs with rotation periods drawn from a source other than the Santos et al. pipeline.

4.2. Planet Quality Flags

Some planets are more reliably identified than others. We used the following additional quality indicators to assess the reliability and utility of a planet, and assembled them into a separate bitmask, Q_{planet} .

*Candidate reliability (bit 0)—The NEA’s Kepler Objects of Interest Table includes both an overall planet-candidate disposition status (*koi_disposition*), as well as a disposition based only on the Kepler data (*koi_pdisposition*). We required both to include only “planet candidates” and “confirmed planets.”*

*Candidate S/N (bit 1)—In any transit survey, the false positive rate increases greatly toward the noise floor for planet detection (e.g. Jenkins et al. 2002). We required a S/N in excess of Kepler’s usual 7.1σ floor, through a cut on the maximum “multiple event statistic” (MES, *koi_max_mult_ev*): we required MES > 10.*

Grazing planets (bit 2)—Grazing objects, for which the impact parameter b is greater than $1 - R_p/R_$, often yield biased planetary parameters (e.g. Gilbert 2022). For large planets, they also include astrophysical false positives at higher rates (Morton et al. 2016), in part due to the size-impact parameter degeneracy. We flagged planet candidates as potentially grazing if $b > 0.8$, using the impact parameters reported by Thompson et al. (2018).*

5. AGES FROM LITHIUM

Figure 3 shows our measured equivalent widths for the lithium 6708 Å absorption doublet, plotted over the mean isochrone models from EAGLES (Jeffries et al. 2023). We show an upper-limit for plotting purposes if the 1σ lower limit on the equivalent width is below 10 mÅ. Our measured EWs span -40 to 250 mÅ; all negative EWs have uncertainties that are statistically consistent with zero.

To calculate lithium ages, we used EAGLES (git commit ac09637), which, similar to *gyro-interp*, is based on an empirical interpolation approach. EAGLES was calibrated on lithium measurements of stars observed by the Gaia-ESO spectroscopic survey in 52 open clusters with ages spanning 2 to 6,000 Myr (Jeffries et al. 2023). We adopted a linear prior in age, spanning 10^6 to 10^{10} yr, and symmetrize our EW uncertainties for purposes of interfacing with EAGLES by taking the maximum of the measured positive and negative 1σ uncertainty intervals.

In part because many of our EWs are upper limits, many of the lithium ages are lower limits. In such cases, the inferred age posterior is strongly influenced by the assumed intrinsic dispersion in the lithium model, and by the prior. In these instances, we quote the 3σ (99.7th percentile) limits.

6. CLUSTER AGE COMPARISON

Stars that formed in the same birth cluster are the gold standard for the astronomical age scale (Soderblom 2010). Before Gaia, the few open clusters known in the Kepler field had been cataloged by Herschel (1864). Gaia has enabled the discovery of new stellar ensembles that are more diffuse, but which nonetheless share a common age based on isochrone, rotation, and lithium dating. Specifically in the Kepler field, NGC6811 (1 Gyr; Curtis et al. 2019) and NGC6819 (2.5 Gyr; Meibom et al. 2015) have been known for centuries, while Theia 520 (≈ 300 Myr; Kounkel & Covey 2019), Melange-3 (≈ 150 Myr; Barber et al. 2022), and Cep-Her (≈ 40 Myr; Bouma et al. 2022b and Kerr et al. 2024) are more recent discoveries.

In Figure 5, we compare our rotation-based ages, and available ages from the literature, against the ages of stars in these open clusters. From the literature, we drew ages from Reinhold & Gizon (2015), Berger et al. (2020b), Lu et al. (2021), Mathur et al. (2023), and Lu et al. (2024). We followed any guidance available from each study for removing ages that were unreliable, and plotted stars within 1σ of zero as upper limits. For the Reinhold & Gizon ages, we used those calculated using the Mamajek & Hillenbrand (2008) calibration; for the Mathur et al. ages, we show those from kiauhoku (Claytor et al. 2020) rather than STAREVOL (Amard et al. 2019), since the former showed better agreement with the cluster age scale.

Cluster membership is a nuanced subject. Figure 5 is showing reported ages for a set of spatially and kinematically selected stars that could be cluster members, or they could be field interlopers. For NGC6811 and NGC6819, we adopted candidate members from Cantat-Gaudin et al. (2018, 2020) and Kounkel et al. (2020). For Theia 520, we used candi-

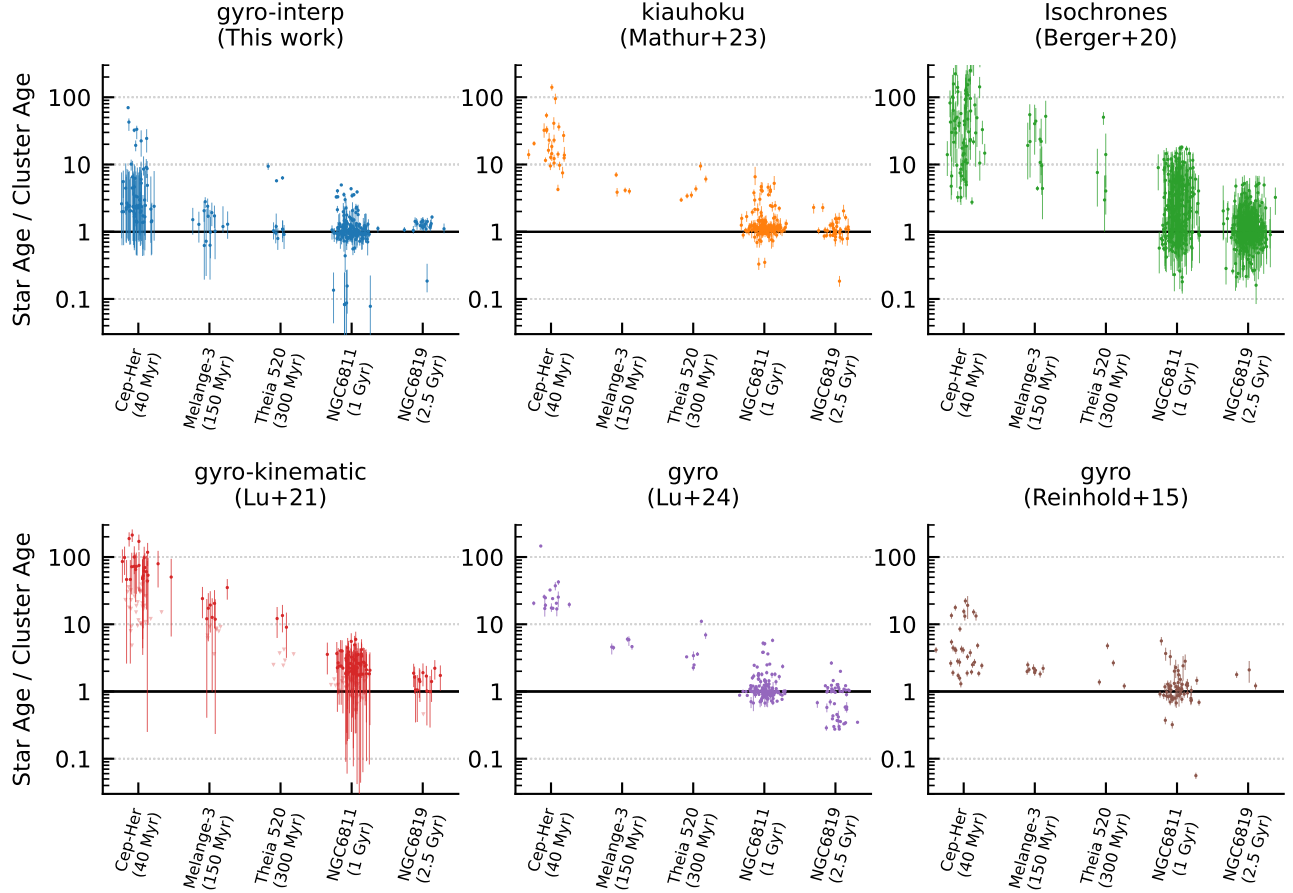


Figure 5. Reported ages of individual stars in benchmark open clusters. Each point denotes a star's reported age, normalized by the age of a stellar ensemble in which the star is a candidate member. Cluster membership was evaluated without knowledge of rotation(Added: , and for this plot, no attempt was made to exclude known binaries). Although some field interlopers may be present in the membership lists, outliers can be compared between different methods on a relative basis. Each study was cross-matched against the same cluster list; certain methods report ages for more stars than others. Horizontal scatter is added to visually clarify the statistical age uncertainties. At <1 Gyr, our ages are generally accurate, and their statistical uncertainties match their dispersion.

date members from Kounkel et al. (2020). For Melange-3, we used the candidates reported by Barber et al. (2022) and required “offset” tangential velocities below 2 km s^{-1} . For Cep-Her, we used candidate members from Kerr et al. 2024 (submitted) with $P_{\text{fin}} > 0.8$. Even with contaminants, we can compare the relative age distributions derived by the different studies because in all instances we are comparing reported ages against a fixed list of stars.

There are two main metrics for success in this test. 1) Do the reported ages agree with the cluster age? 2) Do the reported age uncertainties agree with their dispersion around the cluster age?

Figure 5 show that although previous studies reported ages that agree with the cluster scale for $\gtrsim 1$ Gyr stars, sub-gigayear stars have historically had their ages overestimated by 0.3–2 dex, with severely understated uncertainties. For isochrone and kinematic ages, this is because these methods rely on parameters that do not appreciably change at $t \lesssim 1$ Gyr. For the rotation-based ages in Mathur et al. (2023) and Lu et al. (2024), the discrepancy is caused by details of the cal-

ibration methodologies. The kiauhoku spin-down model for instance has known “stretches” and “compressions” in its age scale relative to observed open clusters (see Mathur et al. 2023, Sec. 7.3). The Mamajek & Hillenbrand (2008) calibration used by Reinhold & Gizon (2015) appears more accurate than the former two models, because it was fitted to reproduce the open cluster sequences known at the time. However, the uncertainties from all of these methods appear to be underestimated. This is probably because they do not marginalize over the range of rotation periods accessible to sub-gigayear stars of a fixed mass and age.

7. RESULTS

7.1. Rotation-Based Age Distribution

7.1.1. Kepler's Demographic Cliff

The stellar ages are given in Table 1 for the known planet hosts, and in Table 2 for all Kepler stars. Figure 6 shows the rotation-based age distributions of all the stars (left column) and the KOI hosts (middle column). These “histograms”

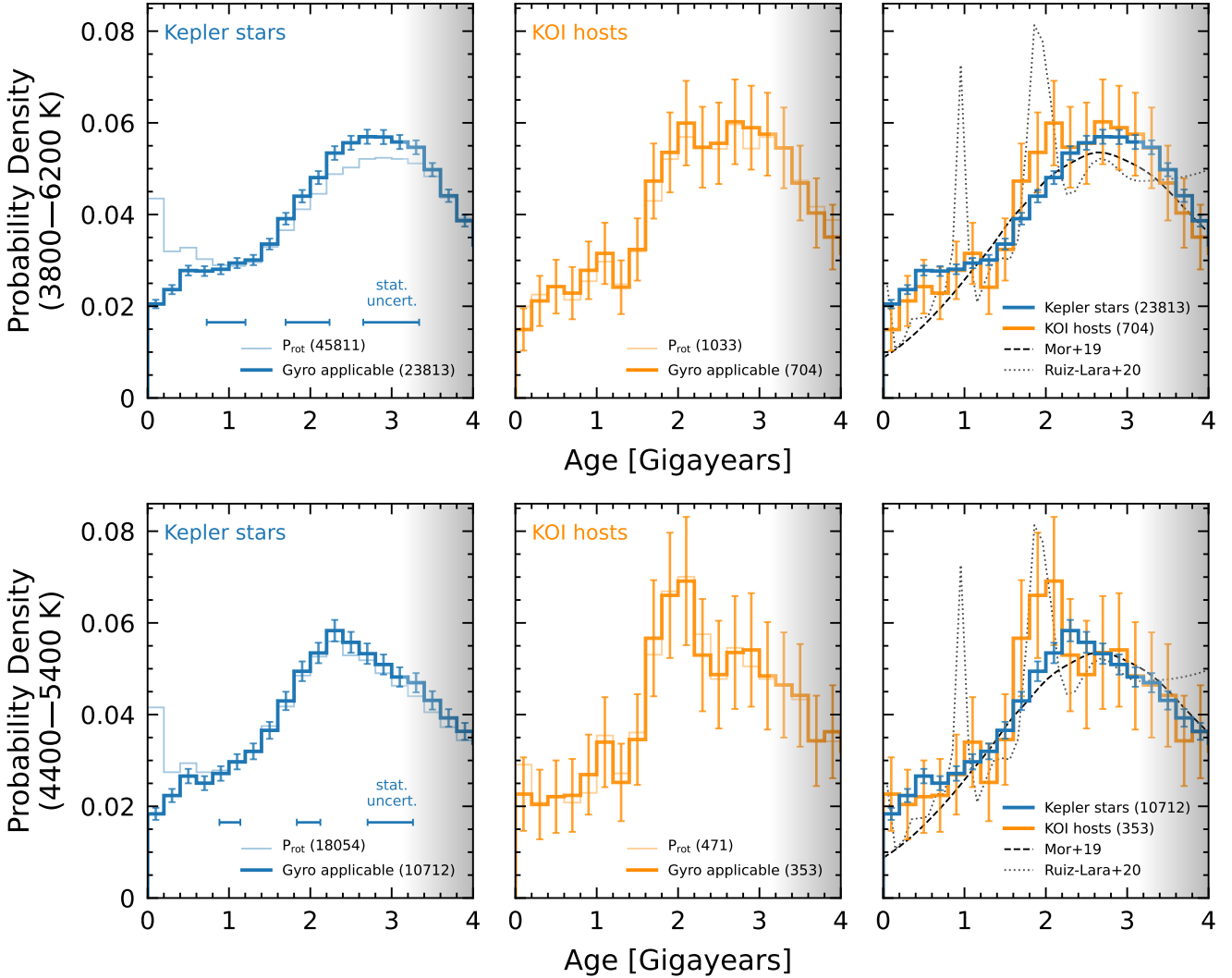


Figure 6. Kepler’s demographic cliff, visible in the rotation-derived age distributions of its stars (left) and planet hosts (middle). The top row shows (Replaced: all stars with temperatures of 3800–6200 K for which we calculated rotational ages replaced with: stars with temperatures of 3800–6200 K). Opaque lines impose quality cuts on binarity, (Added: metallicity,)crowding, and the star’s evolutionary state; transparent lines do not(Added: (see Section 4.1)). The bottom row shows stars with temperatures of 4400–5400 K, which (Replaced: have more precise ages due to their fast spin-down replaced with: have more precise ages). The statistical uncertainty for a mean star at 1, 2, and 3 Gyr is shown, and is identical across each row. Finally, the right panel compares the rotation-derived ages against star formation histories derived using CMD fitting (dashed and dotted lines). Completeness in Kepler’s P_{rot} detection sensitivity is near unity until $t \lesssim 3$ Gyr(Added: , and decreases rapidly at older ages) (Masuda 2022a).

are sampled from the posterior probability distributions by drawing ten random samples from each posterior, and then computing the normalized histogram of the resulting samples. We also considered an alternative approach for constructing these plots using hierarchical Bayesian deconvolution (Masuda et al. 2022), and found similar results. The plotted uncertainties (Replaced: assume Poisson statistics replaced with: are Poissonian). We truncated the plots at 4 Gyr, which is the upper bound for our rotational age calibration. The overall slope (Replaced: yields replaced with: shows) a paucity of young stars relative to the expectation of a uniform age distribution.

The age distributions of Kepler stars and KOI hosts in Figure 6 appear similar. One diagnostic for whether the two distributions are drawn from the same underlying distribution is the Kolmogorov-Smirnov test; we calculated this statistic in a manner that accounts for the Poisson uncertainties by performing 1000 random draws of 70% of the stars from each sample when requiring $t_{\text{gyro}} < 3$ Gyr. The resulting $\log_{10} p$ values spanned (2.5th to 97.5th percentiles) -4.5 to -1.8 for the K dwarfs, and -4.5 to -1.9 for all Kepler stars. This agrees with the visual impression that while small differences may be present, they are not drastic.

The similarity of the KOI host and Kepler star age distributions adds some nuance to the argument that young transiting planets are hard to detect due to the photometric variability of their host stars. If true, this statement (**Replaced:** seems to replaced with: **might**) hold only for the very youngest ($\lesssim 0.4$ Gyr) stars, where there is a marginal deficit in the KOI host age distribution relative to the parent stellar sample. Examining scatter plots of the planet properties as a function of age, we similarly find that fewer systems at $t_{\text{gyro}} < 0.4$ Gyr are detected with $P_{\text{orb}} \gtrsim 30$ days than at $t_{\text{gyro}} > 0.4$ Gyr.

We can quantify the relative counts of stars as a function of age by labelling stars between 0-1 Gyr, 1-2 Gyr, and 2-3 Gyr as “young”, “intermediate-age”, and “old”. A simple counting exercise from Figure 6 tells us that there are 2.1 times as many old stars in the Kepler field as young stars. Similarly, there are 2.6 times as many old planet hosts as young planet hosts. Focusing only on the tails of the distributions (0-0.3 Gyr and 2.7-3 Gyr), the implication is that the formation rate of stars in the Kepler field decreased by a factor of 2.81 ± 0.12 over the past three billion years. If this decrease continues linearly into the future, then a simple extrapolation would imply that in $\approx 1.4 \pm 0.3$ Gyr the rate of new stars forming in the Galaxy will reach zero.

In terms of detected planet counts, our rotation-based ages for the Kepler sample yield {109, 201, 281} detected planets in the 0-1 Gyr, 1-2 Gyr, and 2-3 Gyr bins.

7.1.2. Nuances in the Age Distribution

(**Added:** *Completeness*—Figure 6 has a gray overlay beyond $\gtrsim 3$ Gyr because Kepler’s sensitivity to rotation signals diminishes at old ages.) Masuda (2022a) studied (**Deleted:** this issue)(**Added:** Kepler’s completeness to rotation signals using MIST-derived isochrone ages), and found for Sun-like stars that the fraction of rotation signals (**Added:** that are)detectable (**Deleted:** by Kepler) is near unity up to ≈ 3 Gyr, and that it drops to almost zero by ≈ 5 Gyr. (**Deleted:** This trend is opposite in functional form to our derived age distributions.) (**Added:** This estimate suggests that while aspects of Figure 6 might be interpretable in terms of the Galaxy’s star formation history at $\lesssim 3$ Gyr, at older ages incompleteness precludes any such interpretation.)

(**Added:** *Temperature sensitivity*—There are quantitative differences in Figure 6 between the K dwarfs (4400–5400 K) and the FGK stars (3800–6200 K). For instance, the distribution peaks at 2.3 Gyr for K dwarfs, and at 2.9 Gyr for the FGK sample. The peak is also sharper for the K dwarfs; its decrease from 2.3–3 Gyr is in an age range in which we believe the rotation period catalog completeness to be near unity. We show further details of the $t_{\text{gyro}} - T_{\text{eff}}$ distributions in Appendix D, and propose possible explanations for these differences in Section 8.2.)

7.2. Planets Younger Than One Billion Years

(**Deleted:** Sub-gigayear planets can be particularly informative for studies of planet evolution.) (**Added:** This analysis provides an important path toward expanding the population of young and evolving exoplanets.) Our catalog has 109 confirmed and candidate planets with median ages below 1 Gyr. Requiring $t_{\text{gyro}} < 1$ Gyr at 2σ yields 63 planets orbiting 50 stars. The youth claim is most secure for the systems that are either in clusters (Section 7.2.1), or that have independent rotation and lithium-based ages (Section 7.2.2). These samples provide broader context for the planets around field stars that push the boundaries of the current young exoplanet census (Section 7.2.3).

7.2.1. Planets in Clusters

Four stellar ensembles in the Kepler field have to date yielded a total of fourteen transiting planets. Our analysis blindly recovers the youth of all of these planets.

Cep-Her—The Cep-Her complex (≈ 40 Myr) contains Kepler-1627Ab, Kepler-1643b, Kepler-1974b and Kepler-1975 Ab (Bouma et al. 2022a,b). Different sub-groups of the complex vary in age by $\approx 50\%$ (Kerr et al. 2024). The planets themselves are all on close-in orbits (5–25 days), with sizes from $2\text{--}4 R_{\oplus}$. Our rotation and lithium ages agree with the cluster age for Kepler-1627A, Kepler-1974, and Kepler-1975A. For Kepler-1643, the rotation and cluster ages agree, and the lithium age is 2.0σ above the cluster age reported by Bouma et al. (2022b) for RSG-5.

MELANGE-3—Barber et al. (2022) reported a 105 ± 10 Myr association in the Kepler field containing two transiting mini-Neptunes: Kepler-970 and Kepler-1928. We find rotation-based ages of $t_{\text{gyro}} = 176^{+120}_{-40}$ Myr and 144^{+104}_{-88} Myr for Kepler-970 and Kepler-1928 respectively. The former rotation-based age being slightly older than the suggested Pleiades age for the association agrees with Figure 4 of Barber et al. (2022).

Theia 520—We find rotation-based ages of ≈ 350 Myr for Kepler-968 and Kepler-52. Based on spatial and kinematic clustering, these stars are candidate members of Theia 520 (Kounkel & Covey 2019). The core of this cluster is also known as UBC-1 (Castro-Ginard et al. 2018). Based on isochrone and rotation-based age-dating, Theia 520 seems to be $\approx 230 \pm 70$ Myr old (Fritzewski et al. 2024), which is within 1σ of our t_{gyro} measurements. Ongoing work by Curtis (2024) broadly finds that the two planet-hosting stars are indeed members of this diffuse population. Given the cluster-level and individual-star evidence, this makes Kepler-968 and Kepler-52 the youngest multiplanet systems currently known from the main Kepler mission.

NGC 6811—Meibom et al. (2013) reported the discovery of Kepler-66 and -67b, two mini-Neptunes in NGC 6811 (≈ 1 Gyr). We derive rotation-based ages for these systems of 1431^{+675}_{-364} Myr and 878^{+108}_{-121} Myr for Kepler-66 and -67b, respectively. Kepler-66 ($T_{\text{eff}} \approx 5900$ K, $P_{\text{rot}} \approx 10.4$ days) has a lower precision and a more asymmetric posterior because of its slow spin-down rate. Kepler-67 ($T_{\text{eff}} \approx 5100$ K, $P_{\text{rot}} \approx 10.3$ days) is marginally hotter than the later K dwarfs

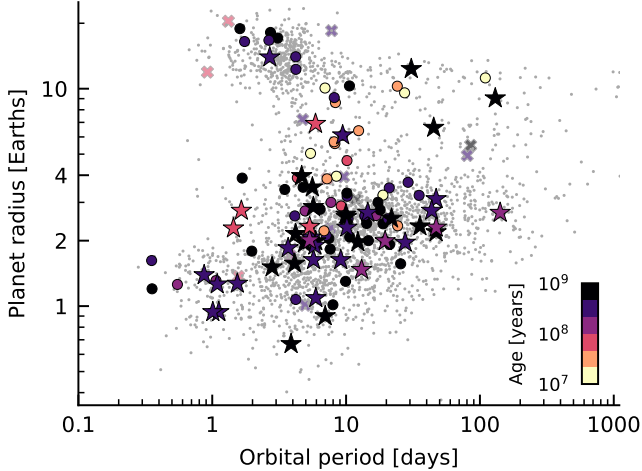


Figure 7. Sizes, orbital periods, and rotation-based ages of transiting exoplanets younger than one billion years. (Replaced: Star symbols denote 46 planets that are characterized in this work to have $t_{\text{gyro}} < 1 \text{ Gyr}$ at 2σ ; circles are planets from the literature meeting the same age requirement, but with a heterogeneous set of age provenances. Gray points are transiting planets from the NASA Exoplanet Archive older than 1 Gyr. If one were to instead select for precise ages ($t/\sigma_t > 3$), this would hide \approx ten $< 0.5 \text{ Gyr}$ planets, and add \approx fifteen $0.5\text{-}1 \text{ Gyr}$ planets. For this plot, we require our Kepler stellar hosts to not have Q_{star} bits 0–9 raised, and for the planets to similarly no have quality flags raised. replaced with: Systems are selected to have $t < 1 \text{ Gyr}$ at 2σ . Star symbols denote 46 planets characterized in this work to have such ages at the highest confidence, meaning that none of Q_{star} bits 0–10 are raised, and the planets have no quality flags raised. Transparent crosses denote 17 planets for which either the planet is grazing, or the star has $\text{RUWE} > 1.4$. Gray points are from the NASA Exoplanet Archive.)

that are in “stalled” spin-down at this time, enabling its rotation period to be diagnostic of its age.

7.2.2. Rotation vs. Lithium Ages

We compared the rotation and lithium ages for the known planet hosts in the “Consistent?” column of Table 1. There were three cases of interest. *i*) If two-sided posteriors for both t_{gyro} and t_{Li} existed, and their median values were consistent within 2σ , we listed them as consistent; if they were consistent within $2\text{-}3\sigma$, we listed them as “maybe” consistent. Otherwise, they disagreed. *ii*) If t_{Li} was a lower limit, we compared this lower limit with the 1σ upper limit from t_{gyro} ; if the two overlapped, we judged the age estimates to be consistent. *iii*) If t_{Li} provided a two-sided posterior, and no rotation period was found, we judged the age estimates to be inconsistent. This is because a two-sided lithium constraint can only be provided for G and K dwarfs $\lesssim 2 \text{ Gyr}$ old, and Kepler should have been sensitive to the rotation periods of such stars.

In the entire planet sample (i.e., without imposing any quality cuts) this yielded 697 consistent cases, 12 maybe

consistent cases, and 22 inconsistent cases. Rephrased, in the overall sample, 95% of stars have consistent rotation and lithium-based ages (97% potentially consistent).

Appendix C describes all cases of “discrepant” confirmed planets for which a sub-gigayear age is reported by at least one age indicator. All but two systems are either evolved stars or else unresolved binaries, and are automatically flagged as such. The more interesting of the two is Kepler-786, an early K dwarf with $t_{\text{Li}} = 228^{+168}_{-87} \text{ Myr}$, but with a $\approx 33 \text{ day}$ rotation period that implies $t_{\text{gyro}} \approx 4.4 \text{ Gyr}$. Other age indicators in the spectrum similarly suggest that the star is not young. It therefore appears to be anomalously lithium-rich.

7.2.3. Notable New Young Planets

Let us focus on blemish-free stars with blemish-free planets: Q_{star} must not have any of bits zero through (Replaced: nine replaced with: ten) raised, and Q_{planet} must similarly have no quality flags raised. Under this constraint, our results include 18 confirmed planets younger than 1 Gyr with two-sided t_{gyro} and t_{Li} , and 37 confirmed planets with comparable ages for which t_{gyro} is two-sided while t_{Li} is one-sided.

Figure 7 shows the planets and planet candidates with $t_{\text{gyro}} < 1 \text{ Gyr}$ at 2σ . (Replaced: This replaced with: The stars in this) figure include (Deleted: s) 37 confirmed Kepler planets, and nine candidate planets, all of which are listed in Table 1. These include four objects Earth-sized or smaller, six Jovian-sized planet candidates, seven super-Neptunes ($4\text{-}10 R_{\oplus}$), 28 mini-Neptunes above the radius valley as parametrized by Van Eylen et al. 2018, and 18 super-Earth sized planets below the radius valley. While most of these planets have orbital periods below 50 days, four are on more distant orbits.

Among these systems, four highlights are Kepler-1529, Kepler-1565, Kepler-1312, and Kepler-1629. Kepler-1529 b is a $\approx 100 \pm 50 \text{ Myr}$ mini-Neptune with well-measured rotation and lithium ages. Kepler-1565 b is an analogous $\approx 170\text{-}230 \text{ Myr}$ super-Earth. Kepler-1312 is a $t_{\text{gyro}} = 357^{+75}_{-109} \text{ Myr}$ near-Solar analog with an Earth-sized planet on a one-day orbit, and a mini-Neptune on a five-day orbit. The Earth-sized planet, Kepler-1312 c, along with the near-identical Kepler-1561 b ($t_{\text{gyro}} = 426^{+74}_{-78} \text{ Myr}$), rank among the youngest Earth-sized planets currently known, comparable to planets such as HD 63433 d ($1.1 R_{\oplus}$, $414 \pm 23 \text{ Myr}$; Capistrant et al. 2024) and TOI-1807 b ($1.3 R_{\oplus}$, $180 \pm 40 \text{ Myr}$; Hedges et al. 2021). Kepler-1629 b, with a size just two-thirds that of Earth ($0.67 \pm 0.05 R_{\oplus}$), is marginally older, also based on rotation ($529^{+62}_{-62} \text{ Myr}$). The lithium age from a reconnaissance TRES spectrum confirms the point.

8. DISCUSSION

8.1. Kinematic Heating and Star Formation in the Thin Disk

(Added: Two separate astrophysical effects might explain our observed age distribution (Figure 6): a declining star formation rate (SFR), and kinematic heating. Kinematic heating is associated with an increase in

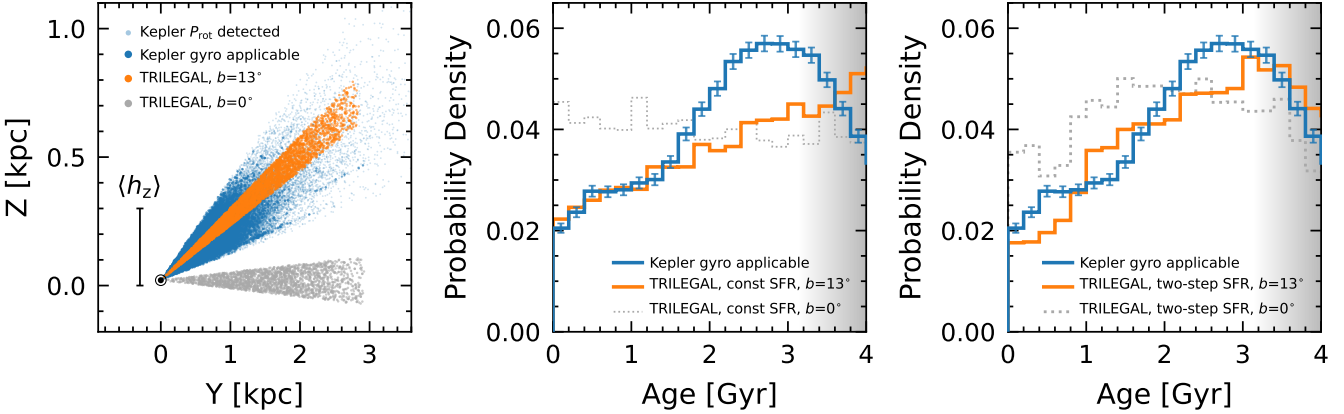


Figure 8. Impact of star formation rate (SFR) and kinematic heating on age distribution. Most Kepler stars are a few hundred parsecs above the Galactic plane (\hat{Z} points to the north galactic pole; \hat{Y} toward the direction of galactic rotation). This is comparable to the ≈ 300 pc mass-weighted scale height. The dotted gray and solid orange lines show synthetic age distributions from TRILEGAL assuming a constant SFR (middle) and a two-step SFR (right), described in the text. A combination of both kinematic heating and a decreasing SFR are needed to qualitatively match the observed paucity of the youngest stars.

both stellar velocity dispersions and the disk's vertical scale height over time (e.g. Villumsen 1983; Schmidt et al. 2024). The Kepler field points toward $(l, b)=(76.3^\circ, 13.5^\circ)$. A typical Kepler star at 1 kpc is therefore ≈ 230 pc above the galactic plane, a significant fraction of the thin disk's mass-weighted ≈ 300 pc scale height (Bland-Hawthorn & Gerhard 2016).)

(Added: We assessed the relative importance of these two effects using the TRILEGAL Monte Carlo population synthesis tool (v1.6; Girardi et al. 2005). (Added: TRILEGAL treats the Galaxy as a linear combination of a thin disk, thick disk, halo, and bulge, and allows for two possible SFRs: constant, and a “two-step” SFR in which the thin disk SFR is 50% larger from 1-4 Gyr than at other ages. This two-step SFR was introduced to improve the model’s ability to match star counts from Hipparcos and 2MASS)(see Section 5.1 of Girardi et al. 2005). (Added: For kinematic heating, TRILEGAL assumes that the disk scale height grows as $h_z = z_0(1+t/t_0)^\alpha$, for $\alpha=5/3$, $z_0=94.7$ pc, and $t_0=5.55$ Gyr, similar to Rana (1991). We queried the web interface toward the Kepler field, and toward the galactic plane (at $l=76.3^\circ$) to negate the effects of kinematic heating. We limited the output to stars with apparent Kepler magnitudes brighter than 16, and set the field of view to 10 deg^2 , the maximum available through the web interface.)

(Added: Figure 8 compares the results against our observed age distribution. The middle panel shows that assuming a constant SFR, kinematic heating alone can yield a two-fold difference in the abundance of the youngest stars relative to those ≈ 3 Gyr old. The right-most panel shows that additionally including the time-variable SFR yields the best agreement with the slope of our observed age distribution.)

(Deleted: Most stars observed by Kepler are in the thin disk. This can be verified by following Gaia Collaboration et al. (2018), and labeling stars with 2D tangential velocities $v_t < 40 \text{ km s}^{-1}$ as thin disk members, and those with $60 < v_t < 150 \text{ km s}^{-1}$ as thick disk members. These criteria yield 95,694 thin and 54,039 thick disk stars observed by Kepler. The thin disk stars have a threefold larger detected rotation period fraction: 35,675 rotators are in the thin disk, while 7,312 are in the thick disk. Further imposing the quality flags discussed in Section 4.1 yields 17,755 thin disk stars for which gyrochronology is applicable, and 2,462 thick disk stars.)

(Deleted: Classifying Kepler stars as thin vs. thick disk members helps connect them to previous work on the Galaxy’s star formation history. On extragalactic scales, the star formation rate in spiral galaxies with mass similar to the Milky Way peaked ≈ 10 Gyr ago, and has since decreased by an order of magnitude.) (Added: Despite the expected differences between pencil-beam surveys and volume-complete samples, our observed age distribution qualitatively agrees with a number of previous studies.) (Replaced: In our own galaxy, previous studies have replaced with: Previous work has) measured star formation histories through CMD fitting of resolved stellar populations (Mor et al. 2019; Ruiz-Lara et al. 2020; Alzate et al. 2021; Xiang & Rix 2022), and by modeling the local white dwarf luminosity function (e.g. Isern 2019). Mor et al. (2019) and Isern (2019) for instance focused on stars (and white dwarfs) within a few hundred parsecs, and both found a peak in the local star formation rate 2-3 Gyr ago. Ruiz-Lara et al. (2020) focused on stars in a wider 2 kpc bubble, and additionally reported three local maxima in the SFR, which they

associated with pericenter passages of the Sagittarius satellite galaxy.

The right column of Figure 6 compares our derived age distribution against star formation histories (SFHs) reported by Mor et al. (2019) and Ruiz-Lara et al. (2020) based on CMD fitting. The overall slope of both SFHs broadly agrees with what we find from rotation-based ages. The SFH from Mor et al. (2019) seems entirely consistent, particularly after accounting for the statistical uncertainties of that study. Regarding the episodic star formation bursts reported by Ruiz-Lara et al. (2020), they are not apparent in our overall FGK star sample (top row). However, rotation-based ages are most precise for \approx G8V-K4V dwarfs older than \approx 1.5 Gyr (Bouma et al. 2023). The lower row of Figure 6 selects these stars with a temperature cut, and may show a (Added: weak)hint of the (Added: \approx 1 Gyr and \approx 2 Gyr spike(Added: s) reported by Ruiz-Lara et al. (2020). (Deleted: The \approx 1 Gyr spike however is not recovered.) This \approx 2.5 Gyr local maximum is similarly present in the isochrone ages derived by Berger et al. (2020b) for the Kepler field, and in the red giant asteroseismic ages derived by Silva Aguirre et al. (2018). The main novelty of our ages relative to (Replaced: those studies is their improved accuracy replaced with: these previous studies is their accuracy) at <1 Gyr(Added: (see Figure 5)).

8.2. Caveats & Limitations

Our most constraining ages tend to come from one source of information: rotation. Factors other than (Deleted: stellar) age and mass can influence (Deleted: stellar) rotation rates. (Added: Astrophysical factors include metallicity, latitudinal differential rotation, mergers, and tidal spin-up. Observational limitations include the difficulty of measuring small-amplitude, long-period signals that are only quasi-coherent due to the starspot lifetime approaching the stellar rotation period. There is also the issue that our age-dating approach is not calibrated beyond 4 Gyr. In the following, we attempt to quantify the importance of these effects in our analysis, ordered by what we perceive to be their descending importance.)

Binaries: Stars in binaries are often biased toward rapid rotation, even beyond the typical realm of tidal synchronization (see Meibom et al. 2007; Gruner et al. 2023). (Added: Simonian et al. (2019) for instance found that 59% of Kepler stars with rotation periods between 1.5 and 7 days lie 0.3 mag above the main sequence, compared with 28% of their full rotation sample. We attempted to mitigate the effects of binarity with five distinct quality flags (Section 4.1). This attempt was at least somewhat effective, based on the peak near zero in the raw distributions of Figure 6 being flattened in the cleaned distributions. However, the completeness of our quality flags is hard to assess. One specific concern is that these flags might have minimal sensitivity to binaries with separations of \approx 0.05–0.5 AU, for all but the highest mass ratios. This inner limit is set by the onset of detectable ellipsoidal variations in Kirk et al. (2016); the outer limit is set by the typical or-

bital periods of astrometric binaries in Gaia DR3)(see Figure 3 of Gaia Collaboration et al. 2023).

(Added: If we were not at all sensitive to binaries with separations of 0.05–0.5 AU, then based on the binary fraction and separation distribution from Raghavan et al. (2010), as much as \approx 5% of our “gyro applicable” sample (1,190/23,813 stars) might be contaminated. In a worst case scenario, all of these unidentified binaries might induce $P_{\text{rot}} < 10$ days, which would then be mixed in with the bona fide young, single stars. This would constitute a major source of contamination, given that our nominal sample of apparently clean stars had 2,706 stars with $P_{\text{rot}} < 10$ days.)

(Added: Figure 9 shows the rotation-based age distribution calculated by randomly dropping 1,190 of the $P_{\text{rot}} < 10$ day stars. Relative to the nominal “gyro applicable” age distribution, there are three important differences. There is a much larger drop in the star formation rate over the past three gigayears, by a factor of 4.81 ± 0.26 , rather than 2.81 ± 0.12 . The rate of decline in star formation since \approx 2.8 Gyr ago is also constant, rather than having a “kink” at 1.5 Gyr. And finally, the corrected distributions show closer agreement with both the SFHs derived from CMD fitting, and also with the KOI host distribution, which is almost devoid of close binaries within 1 AU (e.g. Moe & Kratter 2021, and references therein). We caution however that this correction assumes that *none* of our quality flags were able to identify any of these unresolved binaries. Since we did in fact include flags based on e.g., location in the HR diagram, this correction is best interpreted as an upper limit on the possible impact of binarity.)

(Added: *Rotational outliers:*) We were interested in not only the overall age distribution of the Kepler field, but also in the reliability of individual ages for (Replaced: young stars known to host planets replaced with: each star in our sample). We attempted to assess this reliability using quality bitmasks (Table 1), a comparison against (Deleted: open-)cluster ages (Section 6), and a comparison between rotation and lithium ages. The (Deleted: open-)cluster comparison suggested that our ages were generally accurate at $\ll 0.5$ dex across 0.04–2.5 Gyr, similar to their quoted precision. Nonetheless, the upper-left panel of Figure 5 does show outliers, typically $\lesssim 10\%$ of the population in any cluster. (Added: While most of these outliers are known to have bad quality flags, some do not.) These stars could be either field star contaminants, or else anomalous stars whose physical rotation histories were altered by processes not captured by our statistical uncertainties. Similarly, although we found consistent t_{gyro} and t_{Li} for 18 planets orbiting “high-quality” stars, we did find one system, Kepler-786, with radically different lithium (228^{+168}_{-87} Myr) and rotational (\approx 4.4 Gyr) ages. Planetary mergers are one process that could produce such a

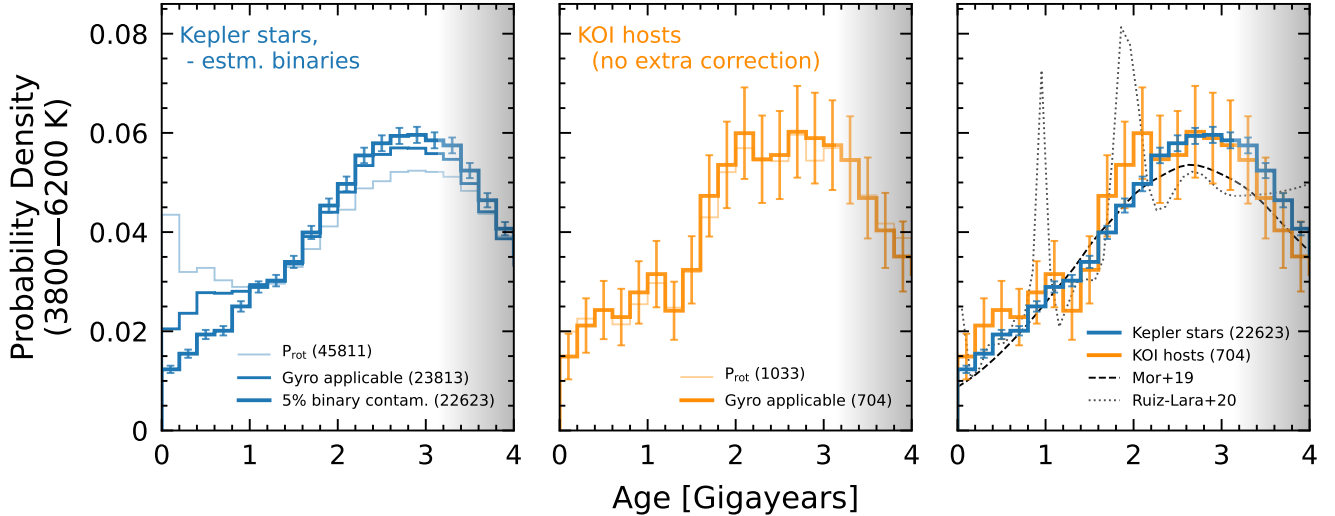


Figure 9. Potential impact of unresolved binaries. This figure shows the same raw (thin blue line) and quality-flag cleaned (“gyro applicable”) distributions as in Figure 6. However, even after applying our quality cuts, up to 1,190 of 2,706 “clean” rotators with $P_{\text{rot}} < 10$ days could be unresolved $\lesssim 0.5$ AU binaries (see Section 8.2). The thick blue “5% binary contamination” distribution corrects for this possibility by randomly removing what we estimate (estm.) to be the maximum possible number of such systems; the true correction might be smaller. We expect such a correction to be more important in the sample of all Kepler stars than in the KOI host sample.

signal, but testing this would require a method for measuring differential abundances across a large number of elements.

(Added: A separate plausible origin for rotational outliers is that they come from erroneously reported rotation periods. While the large surveys do show good internal consistency (Appendix E), the referee correctly pointed out that this is only a comparative test of methods, rather than an ability to recover ground truth (e.g. Aigrain et al. 2015). One could imagine an adversarial scenario in which, say, 10-20% of stars with $P_{\text{rot}} > 20$ days are erroneously reported, and in fact have much longer rotation periods. In this scenario, a similar analysis to that in Figure 9 showed that our analysis would overestimate the degree by which the SFR in the Kepler field has decreased, by 7-14%.)

(Added: Other age indicators may help in verifying the ages of the $\lesssim 3$ Gyr stars that are the main focus of this work. Specifically, chromospheric emission in the X-ray, Ca II HK line, and the UV can serve as an age tracer (Majajek & Hillenbrand 2008; Vidotto et al. 2014; Engle 2024). However, these age indicators are all in a sense “rotation-powered”. The dynamo converts kinetic energy into magnetic energy, which is emitted through these chromospheric pathways. We did not attempt to incorporate these indicators into this study due to concerns regarding sensitivity, homogeneity, and the question of whether they in fact provide age information that is truly independent from rotation.)

(Added: *Weakened magnetic braking:* If we lived in a universe in which stellar rotation rates and spot-induced

photometric amplitudes remained *constant* after ≈ 3 Gyr, then older stars could contaminate the peaks in Figure 6. This scenario deserves consideration, given asteroseismic evidence for slowed spin-down rates after ≈ 4 Gyr for Sun-like stars (van Saders et al. 2016; Hall et al. 2021; Saunders et al. 2024), and the “long-period edge” in the $P_{\text{rot}}\text{-}T_{\text{eff}}$ distribution which may pile up over similar timescales (David et al. 2022). However, the stalling is thought to happen at > 5 Gyr for late-G dwarfs and early K dwarfs (e.g. Figure 4 by Saunders et al. 2024). This means that it cannot explain the 2.3 Gyr peak in the 4400-5400 K age distribution shown in Figure 6. Independently, the study by Masuda (2022a) fitted isochrones to a high-quality subset of Kepler data, and found that the McQuillan et al. (2014) sample, discussed in Appendix E, does not include many stars older than ≈ 4 Gyr. These arguments suggest that the peak in the age distribution is not caused by a pile-up of much older stars with lethargic spin-down rates, but that it could be contaminated by them beyond ≈ 3 Gyr, especially for stars hotter than the Sun.)

(Added: *Metallicity:* Stars with higher metallicity are thought to have longer convective turnover times, which may slow their rate of spin-down (Amard & Matt 2020). While observational studies of this effect have been suggestive, further work remains to definitively establish the importance of the effect (e.g. Amard et al. 2020a; See et al. 2024) Nonetheless, based on the theoretical predictions, we flagged stars with known spectroscopic $[\text{Fe}/\text{H}] > 0.3$, based on either LAMOST or Keck/HIRES spectra (Zong et al. 2018; Petigura et al. 2022). The main limitation of this approach is that only 53.3% of the stars in Ta-

ble 2 with $t_{\text{gyro}} < 4$ Gyr had such spectra available. For the rest of the sample, primarily composed of fainter stars, this means that our quality flags were not sensitive to metallicity outliers. Based on the metallicity distribution of stars for which we do have spectra, this implies that at most $\approx 5\%$ of stars in our sample might have $|\text{[Fe/H]}| > 0.3$, with a slight bias toward lower metallicity stars over higher metallicity. Based on the results by [Claytor et al. \(2020\)](#), this will be most important for stars near the Kraft break, which could have ages overestimated by $\approx 50\text{-}100\%$ if they are in fact metal-poor, and under-estimated in the converse case.)

(Added: Differential rotation: The Sun’s surface rotates once per $\approx 25\text{-}30$ days at latitudes between the equator and $\approx \pm 60^\circ$ ([Snodgrass & Ulrich 1990](#)). This latitudinal surface differential rotation yields two separate limitations on rotational ages. The first is on the accuracy with which any one star’s rotation period can be measured over a few-year mission like Kepler; the second is on the degree to which the intrinsic scatter in open cluster rotation sequences can be measured (e.g. [Epstein & Pinsonneault 2014](#)). In this study, we accounted for the latter intrinsic scatter based on available measurements from Ruprecht-147 ([Curtis et al. 2020](#)) and M67 data ([Barnes et al. 2016; Dungee et al. 2022; Gruner et al. 2023](#)). This means that irrespective of the assumed P_{rot} measurement precision, our model imposed a $\approx 5\text{-}10\%$ level of intrinsic P_{rot} scatter (perhaps differential-rotation induced) at old ages. While this accounts for the statistical impact of differential rotation on the inferred age distribution, the accuracy issue remains; any one individual star’s observed rotation period might be faster or slower than average stars of the same mass and age. This effect can yield a $\approx 20\%$ age bias for individual Sun-like stars with ages of a few billion years; the statistical uncertainties in Table 2 should be treated with appropriate caution.)

(Deleted: Metallicity may also be relevant ([Amard et al. 2020b; See et al. 2024](#)). An additional caveat is that our rotation-based ages used photometric effective temperatures (Section 3), even though spectroscopic temperatures are available for the planet-hosting subset. This decision was driven by a desire for homogeneity irrespective of planet-hosting status. However it implies that the estimated planet ages might shift if one were to account for the spectroscopic information.)

(Deleted: Other age indicators may help in verifying the ages of the $\lesssim 3$ Gyr stars that are the main focus of this work. Specifically, chromospheric emission in the X-ray, Ca II HK line, and the UV can serve as an age tracer ([Mamajek & Hillenbrand 2008; Vidotto et al. 2014; Engle 2024](#)). However, these age indicators are all in a sense “rotation-powered”. The dynamo converts kinetic energy into magnetic energy, which is emitted through

these chromospheric pathways. We did not attempt to incorporate these indicators into this study due to concerns regarding sensitivity, homogeneity, and the question of whether they in fact provide age information that is truly independent from rotation.)

3. Future Directions

(Added: Ages of stars older than the Sun:)(Deleted: A broader question, beyond the scope of this work, concerns the ages of stars $\gtrsim 4$ Gyr old.)(Added: This work was limited to stars younger than 4 Gyr). For age-dating methods based only on rotation rates, an important challenge is that the detectability of the rotation signals for 3-10 Gyr stars, especially Sun-like stars, is at the limits of the Kepler data ([Masuda 2022a](#)). In the “old star” regime, methods that leverage either asteroseismology ([van Saders et al. 2016; Saunders et al. 2024](#)), or else that combine both the evolution of stellar luminosity and stellar rotation ([Angus et al. 2019; Claytor et al. 2020; Mathur et al. 2023](#)) seem the most capable of providing useful age constraints for single stars over the full span of their main-sequence lifetimes.

(Added: Planet) occurrence Rates: The age-dependent trends predicted for exoplanet populations, such as the Kelvin-Helmholtz cooling of mini-Neptunes ([Gupta & Schlichting 2019](#)), time-dependent carving of the photoevaporation desert ([Owen & Lai 2018](#)), and the time evolution of the radius valley ([Rogers & Owen 2021](#)) can be explored using our data. We defer this analysis to a separate publication. Some care is required since beyond age, exoplanet demographics also depend on stellar metallicity and mass (e.g. [Petigura et al. 2018; Miyazaki & Masuda 2023](#)).

Field star ages from other surveys: While this study focused on Kepler, other photometric surveys (e.g. K2, TESS, HAT, WASP, NGTS, ZTF, ATLAS) open opportunities for age-dating a far broader set of stars and planets. Future prospects also include PLATO ([Rauer et al. 2014](#)), Earth 2.0 ([Ge et al. 2022](#)), and the Roman Galactic Bulge Time Domain Survey ([Wilson et al. 2023](#)). Rotation-based age-dating from these surveys could yield new insight into whether the star formation history that we see in the Kepler field is universal across the thin disk.

Searches for new associations: Some of the youngest stars in Tables 1 and 2 have been linked to their birth clusters. Others have not. A systematic search for the birth clusters of the youngest “field stars” could combine positions and velocities from Gaia with rotation measurements from TESS. Given the ~ 100 Myr decoherence time of young clusters, (Replaced: the youngest “field stars” replaced with: these young stars) may have easily identifiable young neighbors.

9. CONCLUSIONS

We began this work with two questions: how wrong is the assumption of a uniform age distribution for stars in the galactic thin disk? And why are only ≈ 50 sub-gigayear transiting planets known, rather than the ≈ 500 that would be

expected under the assumption of a uniform star formation history for the $\approx 5,000$ known planets?

Our approach to answering these questions was to curate a sample of stellar rotation periods, lithium equivalent widths, and temperatures using archival and new data from the Kepler field. We derived new ages using empirical interpolation-based methods, and assessed the reliability of these ages by comparing them against benchmark open clusters (Figure 5).

Tables 1 and 2 summarize the results for planets and stars, respectively. Our recovered ages are accurate for all 14 known Kepler planets in clusters. While lithium provided minimal added information for most of the sample(Added: due to its astrophysical depletion rate), t_{Li} and t_{gyro} agreed in over 90% of cases for which comparison was possible. Our (Replaced: resulting ages replaced with: results) included two-sided t_{gyro} and t_{Li} for 18 sub-gigayear confirmed planets, and two-sided t_{gyro} with one-sided t_{Li} for 37 (Replaced: sub-gigayear confirmed replaced with: such) planets. Allowing for “candidate” planets, grazing transit geometries, and stars with RUWE far from unity expands the counts by a factor of two.

The sizes and periods for the most secure set of planets are shown in Figure 7. While the new young planets are mostly mini-Neptunes, some are near the lower boundary of the “sub-Jovian desert” (Owen & Lai 2018), which could have an evolutionary connection to their youth. Other discoveries include Earth-sized planets (Added: (e.g. Kepler-1312 c and Kepler-1561 b))with (Deleted: new) ages of only a few hundred million years.

Our main conclusions with respect to our original questions are as follows.

1. Rather than being uniform, the age distributions of both the Kepler target stars and the known Kepler planet hosts show a demographic cliff. There are (Added: at least)twice as many “old” (2-3 Gyr) stars in the Kepler field as “young” (0-1 Gyr) stars. (Deleted: The star formation rate today is 2.81 ± 0.12 times lower than it was three billion years ago.)

2. (Added: The youngest stars in the Kepler field (0-0.3 Gyr) are at least 2.81 ± 0.12 times rarer than stars 3 Gyr old. The statistical uncertainty on this value is dwarfed by the systematic uncertainty in the contamination rate of unresolved photometric binaries, which could push it as high as 4.81 ± 0.26 (Section 8.2)). (Replaced: This result replaced with: This range of values) (Replaced: from rotation-based ages broadly agrees replaced with: is broadly consistent) with (Replaced: recent reports of a declining star-formation rate replaced with: modeling expectations (Section 8.1), and with age distributions derived from) from CMD fitting and white-dwarf chronology(Replaced: , though with the replaced with: . The)advantage of (Added: rotation-based ages however is their)(Replaced: sensi-

tivity replaced with: accuracy) for FGK stars at $t < 1$ Gyr (e.g. Figure 5).

- 1287 3. Rather than expecting ≈ 500 exoplanets younger than one
1288 billion years, the age distribution of stars in the Kepler
1289 field (Replaced: implies replaced with: suggests) that we
1290 should instead expect ≈ 250 .
- 1291 4. We have (Replaced: derived replaced with: reported)
1292 rotation-based ages for 63 Kepler planets younger than
1293 1 Gyr at 2σ , and 109 planets with median ages below
1294 1 Gyr. Concatenating these planets against the existing
1295 literature yields ≈ 170 known sub-gigayear planets. This
1296 lessens the original factor of ten discrepancy to a factor of
1297 at most two.
- 1298
- 1299

ACKNOWLEDGMENTS

We thank Kevin Schlaufman and the reviewer for suggestions which significantly improved the manuscript. This work was supported by the Heising-Simons 51 Pegasi b Fellowship (LGB, EKP) and the Arthur R. Adams SURF Fellowship (EKP). The HIRES data were obtained at the Keck Observatory. We recognize the importance that the summit of Maunakea has always had within the indigenous Hawaiian community, and we are deeply grateful for the opportunity to conduct observations from this mountain.

Contributions: Per <https://credit.niso.org/>: Conceptualization: LGB. Data curation: LGB, AWH, HI. Formal analysis: LGB, KM. Funding acquisition: LGB. Investigation: LGB, EKP. Methodology: LGB, EKP, KM. Project administration: LGB, LAH, AWH. Resources: LGB, AWH. Software: LGB. Supervision: LGB, LAH. Validation: LGB, KM. Visualization: LGB. Writing – original draft: LGB. Writing – review & editing: all authors.

Facilities: Gaia (Gaia Collaboration et al. 2022), Kepler (Borucki et al. 2010), Keck:I (HIRES) (Vogt et al. 1994b), 2MASS (Skrutskie et al. 2006), SDSS (York et al. 2000).

Software: astropy (Price-Whelan et al. 2018), clade (Anthropic 2024), eagles (Jeffries et al. 2023), gyro-interp (Bouma et al. 2023), matplotlib (Hunter et al. 2007), numpy (Van Der Walt et al. 2011), scipy (Virtanen et al. 2020).

Table 1. Ages of Kepler planets and planet candidates. This version of the table is truncated to include the youngest systems, sorted by the minimum of either the rotation or lithium-based age. The full machine-readable table contains ages and age limits for 2,461 non-false positive KOIs with MES>10. A bash script to decode the Q_{star} quality flag is [available online](#). A python script to select stars with specific bit flags is [also available](#). All quoted age uncertainties are statistical.

KOI	Kepler	T_{eff}	P_{rot}	EW_{Li}^*	t_{gyro}	t_{Li}	Consistent?	R_p	P_{orb}	Q_{planet}	Q_{star}	Spec?	Comment
-	-	K	days	mÅ	Myr	Myr	str	Earths	days	int	int	bool	-
K05245.01	Kepler-1627 b	5357	2.62	225 ± 7	81^{+158}_{-55}	51^{+38}_{-27}	Yes	3.79	7.2	0	2176	1	Cep-Her
K07368.01	Kepler-1974 b	5068	2.56	248 ± 4	88^{+183}_{-60}	54^{+47}_{-25}	Yes	2.22	6.84	0	2560	1	Cep-Her
K06228.01	Kepler-1644 b	5521	1.43	-2 ± 13	77^{+144}_{-53}	> 767	No	1.88	21.09	4	2690	1	Unres. Binary
K06186.01	Kepler-1643 b	4918	5.05	120 ± 6	79^{+182}_{-54}	191^{+92}_{-76}	Yes	2.11	5.34	0	0	1	Cep-Her
K03933.01	Kepler-1699 b	5496	4.16	-11 ± 7	85^{+106}_{-58}	> 889	No	1.32	3.49	0	2688	1	Unres. Binary
K03916.01	Kepler-1529 b	4974	6.43	200 ± 6	109^{+117}_{-71}	90^{+53}_{-39}	Yes	2.01	5.34	0	0	1	✓✓
K01804.01	Kepler-957 b	4947	4.52	24 ± 9	96^{+196}_{-66}	> 241	Yes	6.9	5.91	0	0	1	✓
K07913.01	Kepler-1975 b	4450	3.36	56 ± 9	96^{+223}_{-66}	> 57	Yes	2.03	24.28	0	2816	1	Cep-Her
K03936.02	Kepler-1930 b	4906	7.1	170 ± 4	174^{+106}_{-65}	115^{+55}_{-49}	Yes	1.52	13.03	4	0	1	
K03876.01	Kepler-1928 b	5577	4.64	137 ± 4	148^{+102}_{-87}	189^{+150}_{-94}	Yes	1.86	19.58	0	2048	1	MELANGE-3
K04069.01	Kepler-1938 b	4617	7.82	6 ± 16	152^{+112}_{-42}	> 208	Yes	1.47	13.06	0	2048	1	✓
K02678.01	Kepler-1313 b	5236	6.13	142 ± 3	197^{+112}_{-91}	174^{+96}_{-72}	Yes	1.71	3.83	4	2048	1	
K04194.01	Kepler-1565 b	4958	7.4	133 ± 7	230^{+111}_{-85}	174^{+81}_{-72}	Yes	1.27	1.54	0	0	1	✓✓
K03835.01	Kepler-1521 b	4806	7.82	117 ± 5	207^{+98}_{-68}	176^{+79}_{-69}	Yes	2.3	47.15	0	2048	1	✓✓
K01838.01	Kepler-970 b	4314	9.23	36 ± 14	177^{+124}_{-39}	> 92	Yes	2.15	16.74	4	0	1	MELANGE-3
K00063.01	Kepler-63 b	5486	5.49	89 ± 4	223^{+98}_{-92}	542^{+475}_{-256}	Yes	5.64	9.43	0	4096	1	✓✓
K01199.01	Kepler-786 b	4680	33.06	83 ± 6	4364^{+359}_{-374}	228^{+168}_{-87}	No	2.31	53.53	0	0	1	Mystery
K03316.01	Kepler-1467 b	5252	6.31	122 ± 6	230^{+112}_{-98}	236^{+151}_{-95}	Yes	3.11	47.06	0	0	1	✓✓
K01074.01	Kepler-762 b	5921	4.01	-27 ± 25	245^{+114}_{-100}	> 548	Maybe	15.19	3.77	0	512	1	
K01839.01	Kepler-971 b	5447	6.22	105 ± 6	306^{+95}_{-115}	366^{+290}_{-164}	Yes	3.93	9.59	0	128	1	
K01833.01	Kepler-968 b	4413	10.46	10 ± 18	328^{+108}_{-87}	> 159	Yes	1.85	3.69	0	0	1	Theia-520
K01833.03	Kepler-968 c	4413	10.46	10 ± 18	328^{+108}_{-87}	> 159	Yes	1.63	5.71	0	0	1	Theia-520
K01833.02	Kepler-968 d	4413	10.46	10 ± 18	328^{+108}_{-87}	> 159	Yes	2.28	7.68	4	0	1	Theia-520
K02675.01	Kepler-1312 b	5584	6.13	86 ± 4	357^{+75}_{-109}	642^{+617}_{-318}	Yes	2.07	5.45	0	4096	1	✓✓
K02675.02	Kepler-1312 c	5584	6.13	86 ± 4	357^{+75}_{-109}	642^{+617}_{-318}	Yes	0.94	1.12	0	4096	1	✓✓
K00775.02	Kepler-52 b	4164	11.85	22 ± 18	360^{+208}_{-97}	> 100	Yes	2.19	7.88	0	0	1	Theia-520
K00775.01	Kepler-52 c	4164	11.85	22 ± 18	360^{+208}_{-97}	> 100	Yes	2.04	16.38	0	0	1	Theia-520
K00775.03	Kepler-52 d	4164	11.85	22 ± 18	360^{+208}_{-97}	> 100	Yes	2.03	36.45	0	0	1	Theia-520
K04004.01	Kepler-1933 b	5576	6.21	85 ± 3	366^{+74}_{-109}	642^{+603}_{-318}	Yes	1.01	4.94	4	0	1	
K02174.03	Kepler-1802 b	4245	11.45	–	379^{+201}_{-109}	–	–	1.71	7.73	4	820	0	
K02174.02	Kepler-1802 c	4245	11.45	–	379^{+201}_{-109}	–	–	2.05	33.14	0	820	0	
K03935.01	Kepler-1532 b	5554	6.48	90 ± 6	397^{+71}_{-102}	567^{+545}_{-278}	Yes	1.26	1.09	0	0	1	✓✓
K01801.01	Kepler-955 b	5221	7.5	79 ± 4	397^{+99}_{-131}	536^{+481}_{-237}	Yes	2.69	14.53	0	0	1	✓✓
K01800.01	Kepler-447 b	5648	6.4	103 ± 3	420^{+64}_{-78}	405^{+355}_{-203}	Yes	18.49	7.79	4	2048	1	
K03370.02	Kepler-1481 b	4832	9.11	22 ± 7	407^{+126}_{-118}	> 210	Yes	1.09	5.94	0	0	1	✓
K04156.01	Kepler-1943 b	6002	–	99 ± 5	–	409^{+520}_{-254}	No	1.29	4.85	4	518	1	
K00448.01	Kepler-159 b	4511	10.5	19 ± 10	415^{+160}_{-110}	> 161	Yes	2.3	10.14	0	4096	1	✓
K00448.02	Kepler-159 c	4511	10.5	19 ± 10	415^{+160}_{-110}	> 161	Yes	2.75	43.59	0	4096	1	✓
K00046.01	Kepler-101 b	5498	–	100 ± 5	–	419^{+349}_{-196}	No	5.9	3.49	0	1542	1	
K04169.01	Kepler-1561 b	5742	6.18	66 ± 3	426^{+74}_{-78}	1409^{+1718}_{-788}	Maybe	0.94	1.01	0	2048	1	✓✓
K02708.01	Kepler-1320 b	4536	10.46	25 ± 32	430^{+173}_{-113}	> 140	Yes	1.39	0.87	0	0	1	✓
K00119.01	Kepler-108 b	5626	–	100 ± 5	–	438^{+402}_{-220}	No	8.2	49.18	0	418	1	
K00119.02	Kepler-108 c	5626	–	100 ± 5	–	438^{+402}_{-220}	No	7.78	190.32	4	418	1	
K00323.01	Kepler-523 b	5267	7.6	49 ± 4	444^{+87}_{-114}	1824^{+2706}_{-1047}	Maybe	1.9	5.84	0	0	1	✓✓
K02115.01	Kepler-67 b	5126	10.39	83 ± 10	878^{+108}_{-121}	458^{+451}_{-206}	Yes	2.96	15.73	0	0	1	✓✓
K00002.01	Kepler-2 b	6436	–	83 ± 4	–	485^{+924}_{-535}	–	16.42	2.2	0	7	1	
K03371.02	Kepler-1482 b	5330	7.7	52 ± 3	491^{+76}_{-91}	1630^{+2285}_{-904}	Maybe	1.0	12.25	0	640	1	

Table 1 *continued*

Table 1 (continued)

K03497.01	Kepler-1512 b	4894	9.33	14 ± 8	505^{+135}_{-115}	> 295	Yes	0.8	20.36	4	4738	1
K03864.01	Kepler-1698 b	4866	9.49	2 ± 8	518^{+151}_{-123}	> 358	Yes	0.9	1.21	0	1024	1
K03010.01	Kepler-1410 b	3808	14.19	-21 ± 24	523^{+612}_{-196}	> 80	Yes	1.39	60.87	0	512	1
K05447.02	Kepler-1629 b	5585	7.45	–	529^{+62}_{-62}	–	–	0.67	3.88	0	0	0
K04246.01	Kepler-1576 b	5794	7.09	17 ± 8	559^{+103}_{-71}	> 613	Yes	0.9	6.98	0	0	1
K03324.01	Kepler-1469 b	5356	8.15	-5 ± 25	562^{+75}_{-82}	> 535	Yes	2.53	21.86	0	0	1
K01779.01	Kepler-318 b	5799	7.09	65 ± 3	562^{+106}_{-72}	1507^{+1876}_{-858}	Yes	3.97	4.66	0	0	1
K01779.02	Kepler-318 c	5799	7.09	65 ± 3	562^{+106}_{-72}	1507^{+1876}_{-858}	Yes	3.1	11.82	4	0	1
K02084.01	Kepler-1792 b	4942	9.49	13 ± 11	587^{+155}_{-144}	> 312	Yes	2.15	4.2	0	0	1
K02035.01	Kepler-1066 b	5847	7.0	60 ± 4	588^{+158}_{-85}	2018^{+2616}_{-1187}	Maybe	1.96	1.93	4	1024	1
K03274.01	Kepler-1451 b	5675	7.82	42 ± 4	597^{+79}_{-65}	> 316	Yes	2.33	35.62	0	0	1
K01615.01	Kepler-908 b	5670	7.88	67 ± 4	602^{+77}_{-65}	1317^{+1607}_{-724}	Yes	1.36	1.34	0	4608	1
K02022.01	Kepler-349 b	5756	7.71	64 ± 6	617^{+103}_{-72}	1686^{+2185}_{-976}	Yes	1.99	5.93	0	0	1
K02022.02	Kepler-349 c	5756	7.71	64 ± 6	617^{+103}_{-72}	1686^{+2185}_{-976}	Yes	1.97	12.25	0	0	1
K00620.01	Kepler-51 b	5635	8.14	48 ± 8	623^{+75}_{-65}	> 258	Yes	6.62	45.16	0	0	1
K00620.03	Kepler-51 c	5635	8.14	48 ± 8	623^{+75}_{-65}	> 258	Yes	5.49	85.32	4	0	1
K00620.02	Kepler-51 d	5635	8.14	48 ± 8	623^{+75}_{-65}	> 258	Yes	9.04	130.18	0	0	1
K02803.01	Kepler-1877 b	5506	8.37	3 ± 12	624^{+69}_{-65}	> 726	Maybe	0.55	2.38	0	1024	1
K00720.04	Kepler-221 b	5070	9.3	21 ± 5	636^{+120}_{-115}	> 341	Yes	1.51	2.8	0	0	1
K00720.01	Kepler-221 c	5070	9.3	21 ± 5	636^{+120}_{-115}	> 341	Yes	2.86	5.69	0	0	1
K00720.02	Kepler-221 d	5070	9.3	21 ± 5	636^{+120}_{-115}	> 341	Yes	2.57	10.04	0	0	1
K00720.03	Kepler-221 e	5070	9.3	21 ± 5	636^{+120}_{-115}	> 341	Yes	2.58	18.37	4	0	1
K03097.02	Kepler-431 b	6259	16.16	80 ± 3	–	671^{+1092}_{-458}	–	0.93	6.8	4	4103	1
K03097.03	Kepler-431 c	6259	16.16	80 ± 3	–	671^{+1092}_{-458}	–	0.93	8.7	4	4103	1
K03097.01	Kepler-431 d	6259	16.16	80 ± 3	–	671^{+1092}_{-458}	–	1.08	11.92	4	4103	1
K01982.01	Kepler-1781 b	5363	9.17	–	708^{+80}_{-78}	–	–	1.95	4.89	0	0	0
K03375.01	Kepler-1918 b	5522	9.11	–	722^{+75}_{-71}	–	–	2.19	47.06	0	0	0
K01835.02	Kepler-326 b	5142	9.56	8 ± 8	724^{+108}_{-103}	> 506	Yes	1.25	2.25	0	1664	1
K01835.01	Kepler-326 c	5142	9.56	8 ± 8	724^{+108}_{-103}	> 506	Yes	1.38	4.58	0	1664	1
K01835.03	Kepler-326 d	5142	9.56	8 ± 8	724^{+108}_{-103}	> 506	Yes	1.31	6.77	0	1664	1
K01797.01	Kepler-954 b	4736	10.68	4 ± 11	727^{+222}_{-184}	> 270	Yes	2.16	16.78	0	1024	1
K01821.01	Kepler-963 b	5383	9.42	–	748^{+80}_{-78}	–	–	2.64	9.98	0	0	0
K03681.01	Kepler-1514 b	5852	7.87	69 ± 2	758^{+416}_{-142}	1302^{+1622}_{-754}	Yes	11.94	217.83	0	1540	1
K03681.02	Kepler-1514 c	5852	7.87	69 ± 2	758^{+416}_{-142}	1302^{+1622}_{-754}	Yes	1.17	10.51	4	1540	1
K00647.01	Kepler-634 b	6272	–	77 ± 3	–	768^{+1250}_{-527}	–	2.13	5.17	0	7	1
K02037.01	Kepler-1995 b	4746	10.8	9 ± 21	772^{+213}_{-194}	> 223	Yes	3.46	73.76	0	4096	1
K01781.02	Kepler-411 b	4920	10.32	4 ± 3	775^{+164}_{-166}	> 396	Yes	2.2	3.01	4	0	1
K01781.01	Kepler-411 c	4920	10.32	4 ± 3	775^{+164}_{-166}	> 396	Yes	3.47	7.83	0	0	1
K07375.01	–	4212	3.88	117 ± 9	104^{+235}_{-72}	70^{+37}_{-21}	Yes	1.73	4.85	0	2560	1
K03991.01	–	5226	5.22	98 ± 3	71^{+91}_{-48}	354^{+253}_{-145}	Maybe	1.37	1.57	0	2176	1
K01546.01	–	5639	0.9	33 ± 24	75^{+134}_{-51}	> 316	Maybe	11.92	0.92	0	2176	1
K05482.01	–	5519	0.81	–	77^{+144}_{-53}	–	–	2.96	31.71	4	2690	0
K00064.01	–	5306	2.23	3 ± 4	81^{+129}_{-55}	> 567	No	10.49	1.95	4	4614	1
K06188.01	–	5209	1.62	6 ± 11	84^{+171}_{-58}	> 554	Maybe	2.75	1.65	0	2048	1
K02695.01	–	5174	2.88	–	86^{+176}_{-59}	–	–	20.23	2.5	4	640	0
K07449.01	–	4928	1.31	–	92^{+194}_{-63}	–	–	20.43	1.32	4	2048	0
K06130.01	–	4560	3.02	-1 ± 25	94^{+217}_{-65}	> 186	Yes	1.45	1.54	0	2976	1
K06195.01	–	4677	1.42	-8 ± 30	94^{+210}_{-65}	> 208	Yes	2.28	1.44	0	2048	1

NOTE—EW_{Li}* is the lithium equivalent width *after* subtracting a constant 7.5 mÅ to account for the Fe I 6707.44 Å blend (see Section 2.3). Two checkmarks (✓✓) denote confirmed planets with two-sided t_{gyro} and t_{Li} for which both the age and the planet are expected to be reliable. One checkmark (✓) denotes confirmed planets with two-sided t_{gyro} only. “Confirmed” planets appear in the machine-readable version before “candidate” planets. Planetary sizes are mostly drawn from (in order of precedence) Petigura et al. (2022), Berger et al. (2020a), and Thompson et al. (2018), and might be unphysical for grazing planets. The bit quality flags for the rotation-based ages, Q_{star} , are described in Section 4.1. Concisely summarized, they are: Bit 0: $T_{\text{eff}}/\text{K} \in [3800 - 6200]$? Bit 1: $\log g < 4.2$? Bit 2: $M_{\text{G}} < 3.9$ or $M_{\text{G}} > 8.5$? Bit 3: In KEBC? Bit 4: Large $d_{\text{xm}, \text{Kep-Gaia}}$? Bit 5: Confused Kep-Gaia crossmatch? Bit 6: Gaia DR3 non-single star? Bit 7: RUWE > 1.4? Bit 8: Crowded? Bit 9: Far from main sequence? Bit 10: Spectroscopic $[\text{Fe}/\text{H}] > 0.3$? Bit 11: S21 CP/CB? Bit 12: P_{rot} not in the homogeneous S19 S21 sample? As an example, Kepler-1627 has Q_{star} flagged with bit 11 and bit 7. The analogous planet quality bitmask, Q_{planet} , has the following meaning. Bit 0: Candidate not reliable? Bit 1: MES < 10? Bit 2: Grazing? For a star to have a high likelihood of being “reliable for gyrochronology” we suggest a Q_{star} bitmask with bits 0–10 not raised, and for a planet to be “reliable”, we suggest Q_{planet} to be zero.

Table 2. Ages of Kepler target stars derived from rotation periods. The full machine-readable table includes 37,892 stars with finite reported gyrochrone ages. The quality bitmask is as in Table 1; requiring bits zero to ten to be null yields 23,813 stars for which gyrochronology is likely to be valid.

KIC	Gaia DR3	T_{eff}	P_{rot}	t_{gyro}	Q_{star}
–	–	K	days	Myr	int
8367679	2126373303927600000	5980	7.44	1062 ⁺⁸¹⁵ ₋₃₆₉	0
11954016	2133663925009149952	5423	24.88	3230 ⁺³³⁰ ₋₃₀₁	0
1865152	2051034045638265984	5878	7.67	879 ⁺⁸⁹¹ ₋₂₇₄	0
4447913	2100652256617096832	4654	35.67	> 4000	0
11085139	2129657064120722688	5507	20.49	2596 ⁺³²² ₋₂₆₇	0

REFERENCES

- 1315 Aigrain, S., Llama, J., Ceillier, T., et al. 2015, MNRAS, 450, 3211
- 1316 Akeson, R. L., Chen, X., Ciardi, D., et al. 2013, PASP, 125, 989
- 1317 Alzate, J. A., Bruzual, G., & Díaz-González, D. J. 2021, MNRAS, 501, 302
- 1318 Amard, L., & Matt, S. P. 2020, ApJ, 889, 108
- 1319 Amard, L., Palacios, A., Charbonnel, C., et al. 2019, A&A, 631, A77
- 1320 Amard, L., Roquette, J., & Matt, S. P. 2020a, MNRAS, 499, 3481
- 1321 —. 2020b, MNRAS, 499, 3481
- 1322 Angus, R., Aigrain, S., Foreman-Mackey, D., & McQuillan, A. 2015, MNRAS, 450, 1787
- 1323 Angus, R., Morton, T., Aigrain, S., Foreman-Mackey, D., & Rajpaul, V. 2018, MNRAS, 474, 2094
- 1324 Angus, R., Morton, T. D., Foreman-Mackey, D., et al. 2019, AJ, 158, 173
- 1325 Anthropic. 2024, Claude, v3, Anthropic, Conversational AI model used for editing manuscript and generating testable code; the authors wrote all of the original manuscript text.
- 1326 <https://claude.ai/>
- 1327 Barber, M. G., Mann, A. W., Bush, J. L., et al. 2022, AJ, 164, 88
- 1328 Barnes, S. A. 2003, ApJ, 586, 464
- 1329 Barnes, S. A., Weingrill, J., Fritzewski, D., Strassmeier, K. G., & Platais, I. 2016, ApJ, 823, 16
- 1330 Berger, T. A., Howard, A. W., & Boesgaard, A. M. 2018, ApJ, 855, 115
- 1331 Berger, T. A., Huber, D., Gaidos, E., van Saders, J. L., & Weiss, L. M. 2020a, AJ, 160, 108
- 1332 Berger, T. A., Huber, D., van Saders, J. L., et al. 2020b, AJ, 159, 280
- 1333 Binney, J., Dehnen, W., & Bertelli, G. 2000, MNRAS, 318, 658
- 1334 Bland-Hawthorn, J., & Gerhard, O. 2016, ARA&A, 54, 529
- 1335 Bonomo, A. S., Sozzetti, A., Lovis, C., et al. 2014, A&A, 572, A2
- 1336 Borucki, W. J., Koch, D., Basri, G., et al. 2010, Science, 327, 977
- 1337 Bouma, L. G., Curtis, J. L., Hartman, J. D., Winn, J. N., & Bakos, G. Á. 2021, AJ, 162, 197
- 1338 Bouma, L. G., Palumbo, E. K., & Hillenbrand, L. A. 2023, ApJL, 947, L3
- 1339 Bouma, L. G., Hartman, J. D., Brahm, R., et al. 2020, AJ, 160, 239
- 1340 Bouma, L. G., Curtis, J. L., Masuda, K., et al. 2022a, AJ, 163, 121
- 1341 Bouma, L. G., Kerr, R., Curtis, J. L., et al. 2022b, AJ, 164, 215
- 1342 Boyle, A. W., & Bouma, L. G. 2023, AJ, 166, 14
- 1343 Cantat-Gaudin, T., Jordi, C., Vallenari, A., et al. 2018, A&A, 618, A93
- 1344 Cantat-Gaudin, T., Anders, F., Castro-Ginard, A., et al. 2020, A&A, 640, A1
- 1345 Capistrant, B. K., Soares-Furtado, M., Vanderburg, A., et al. 2024, AJ, 167, 54
- 1346 Carlos, M., Meléndez, J., Spina, L., et al. 2019, MNRAS, 485, 4052
- 1347 Castro-Ginard, A., Jordi, C., Luri, X., et al. 2018, A&A, 618, A59
- 1348 Chaboyer, B., Demarque, P., & Pinsonneault, M. H. 1995, ApJ, 441, 865
- 1349 Chiti, F., van Saders, J. L., Heintz, T. M., et al. 2024, arXiv e-prints, arXiv:2403.12129
- 1350 Choi, J., Dotter, A., Conroy, C., et al. 2016, ApJ, 823, 102
- 1351 Christiansen, J. L., Zink, J. K., Hardegree-Ullman, K. K., et al. 2023, AJ, 166, 248
- 1352 Claytor, Z. R., van Saders, J. L., Santos, Å. R. G., et al. 2020, ApJ, 888, 43
- 1353 Curtis, J. 2024, in American Astronomical Society Meeting Abstracts, Vol. 243, American Astronomical Society Meeting Abstracts, 458.08

- 1377 Curtis, J. L., Agüeros, M. A., Douglas, S. T., & Meibom, S. 2019,
1378 ApJ, 879, 49
- 1379 Curtis, J. L., Vanderburg, A., Torres, G., et al. 2018, AJ, 155, 173
- 1380 Curtis, J. L., Agüeros, M. A., Matt, S. P., et al. 2020, ApJ, 904, 140
- 1381 David, T. J., Angus, R., Curtis, J. L., et al. 2022, ApJ, 933, 114
- 1382 David, T. J., Petigura, E. A., Luger, R., et al. 2019, ApJL, 885, L12
- 1383 David, T. J., Contardo, G., Sandoval, A., et al. 2021, AJ, 161, 265
- 1384 Denissenkov, P. A., Pinsonneault, M., Terndrup, D. M., &
1385 Newsham, G. 2010, ApJ, 716, 1269
- 1386 Dotter, A. 2016, ApJS, 222, 8
- 1387 Dungee, R., van Saders, J., Gaidos, E., et al. 2022, ApJ, 938, 118
- 1388 Engle, S. G. 2024, ApJ, 960, 62
- 1389 Engle, S. G., & Guinan, E. F. 2023, ApJL, 954, L50
- 1390 Epstein, C. R., & Pinsonneault, M. H. 2014, ApJ, 780, 159
- 1391 Fortney, J. J., Marley, M. S., & Barnes, J. W. 2007, ApJ, 659, 1661
- 1392 Fritzewski, D. J., Barnes, S. A., James, D. J., & Strassmeier, K. G.
1393 2021, A&A, 652, A60
- 1394 Fritzewski, D. J., Van Reeth, T., Aerts, C., et al. 2024, A&A, 681,
1395 A13
- 1396 Fulton, B. J., & Petigura, E. A. 2018, AJ, 156, 264
- 1397 Fulton, B. J., Petigura, E. A., Howard, A. W., et al. 2017, AJ, 154,
1398 109
- 1399 Gaia Collaboration, Babusiaux, C., van Leeuwen, F., et al. 2018,
1400 A&A, 616, A10
- 1401 Gaia Collaboration, Vallenari, A., Brown, A. G. A., et al. 2022,
1402 arXiv e-prints, arXiv:2208.00211
- 1403 Gaia Collaboration, Arenou, F., Babusiaux, C., et al. 2023, A&A,
1404 674, A34
- 1405 Gallet, F., & Bouvier, J. 2015, A&A, 577, A98
- 1406 Ge, J., Zhang, H., Zang, W., et al. 2022, arXiv e-prints,
1407 arXiv:2206.06693
- 1408 Gilbert, G. J. 2022, AJ, 163, 111
- 1409 Gillen, E., Briegal, J. T., Hodgkin, S. T., et al. 2020, MNRAS, 492,
1410 1008
- 1411 Girardi, L., Groenewegen, M. A. T., Hatziminaoglou, E., & da
1412 Costa, L. 2005, A&A, 436, 895
- 1413 Green, G. M., Schlafly, E., Zucker, C., Speagle, J. S., &
1414 Finkbeiner, D. 2019, ApJ, 887, 93
- 1415 Greiss, S., Steeghs, D., Gänsicke, B. T., et al. 2012, AJ, 144, 24
- 1416 Gruner, D., Barnes, S. A., & Weingrill, J. 2023, A&A, 672, A159
- 1417 Gupta, A., & Schlichting, H. E. 2019, MNRAS, 487, 24
- 1418 Hall, O. J., Davies, G. R., van Saders, J., et al. 2021, Nature
1419 Astronomy, 5, 707
- 1420 Hedges, C., Hughes, A., Zhou, G., et al. 2021, AJ, 162, 54
- 1421 Herschel, J. F. W. 1864, Philosophical Transactions of the Royal
1422 Society of London Series I, 154, 1
- 1423 Huber, D., Chaplin, W. J., Christensen-Dalsgaard, J., et al. 2013,
1424 ApJ, 767, 127
- 1425 Huber, D., Zinn, J., Bojsen-Hansen, M., et al. 2017, ApJ, 844, 102
- 1426 Hunter, J. D., et al. 2007, Computing in science and engineering, 9,
1427 90
- 1428 Isern, J. 2019, ApJL, 878, L11
- 1429 Izidoro, A., Ogihara, M., Raymond, S. N., et al. 2017, MNRAS,
1430 470, 1750
- 1431 Jeffries, R. D., Jackson, R. J., Wright, N. J., et al. 2023, MNRAS,
1432 523, 802
- 1433 Jenkins, J. M., Caldwell, D. A., & Borucki, W. J. 2002, ApJ, 564,
1434 495
- 1435 Johnson, J. A., Petigura, E. A., Fulton, B. J., et al. 2017, AJ, 154,
1436 108
- 1437 Kawaler, S. D. 1989, ApJL, 343, L65
- 1438 Kepler, M., Benisty, M., Müller, A., et al. 2018, A&A, 617, A44
- 1439 Kerr, R., Kraus, A. L., Krolikowski, D., Bouma, L. G., & Farias,
1440 J. P. 2024, arXiv e-prints, arXiv:2406.19530
- 1441 Kerr, R. M. P., Rizzuto, A. C., Kraus, A. L., & Offner, S. S. R.
1442 2021, ApJ, 917, 23
- 1443 Kipping, D., & Bakos, G. 2011, ApJ, 733, 36
- 1444 Kirk, B., Conroy, K., Prša, A., et al. 2016, AJ, 151, 68
- 1445 Klein, B., Zicher, N., Kavanagh, R. D., et al. 2022, MNRAS, 512,
1446 5067
- 1447 Kolbl, R., Marcy, G. W., Isaacson, H., & Howard, A. W. 2015, AJ,
1448 149, 18
- 1449 Kounkel, M., & Covey, K. 2019, AJ, 158, 122
- 1450 Kounkel, M., Covey, K., & Stassun, K. G. 2020, AJ, 160, 279
- 1451 Livingston, J. H., Dai, F., Hirano, T., et al. 2018, AJ, 155, 115
- 1452 Lu, Y., Angus, R., Foreman-Mackey, D., & Hattori, S. 2024, AJ,
1453 167, 159
- 1454 Lu, Y. L., Angus, R., Curtis, J. L., David, T. J., & Kiman, R. 2021,
1455 AJ, 161, 189
- 1456 Lu, Y. L., Curtis, J. L., Angus, R., David, T. J., & Hattori, S. 2022,
1457 AJ, 164, 251
- 1458 Mamajek, E. E., & Hillenbrand, L. A. 2008, ApJ, 687, 1264
- 1459 Mann, A. W., Gaidos, E., Mace, G. N., et al. 2016, ApJ, 818
- 1460 Marois, C., Macintosh, B., Barman, T., et al. 2008, Science, 322,
1461 1348
- 1462 Masuda, K. 2014, ApJ, 783, 53
- 1463 —. 2022a, ApJ, 937, 94
- 1464 —. 2022b, ApJ, 933, 195
- 1465 Masuda, K., Petigura, E. A., & Hall, O. J. 2022, MNRAS, 510,
1466 5623
- 1467 Mathur, S., Huber, D., Batalha, N. M., et al. 2017, ApJS, 229, 30
- 1468 Mathur, S., Claytor, Z. R., Santos, Á. R. G., et al. 2023, ApJ, 952,
1469 131
- 1470 Matt, S. P., Brun, A. S., Baraffe, I., Bouvier, J., & Chabrier, G.
1471 2015, ApJL, 799, L23
- 1472 Mazeh, T., Perets, H. B., McQuillan, A., & Goldstein, E. S. 2015,
1473 ApJ, 801, 3
- 1474 McQuillan, A., Mazeh, T., & Aigrain, S. 2013, ApJL, 775, L11
- 1475 —. 2014, ApJS, 211, 24

- 1476 Meibom, S., Barnes, S. A., Platais, I., et al. 2015, *Nature*, 517, 589
- 1477 Meibom, S., Mathieu, R. D., & Stassun, K. G. 2007, *ApJL*, 665, L155
- 1478
- 1479 Meibom, S., Torres, G., Fressin, F., et al. 2013, *Nature*, 499, 55
- 1480 Mills, S. M., & Fabrycky, D. C. 2017, *AJ*, 153, 45
- 1481 Miyazaki, S., & Masuda, K. 2023, *AJ*, 166, 209
- 1482 Moe, M., & Kratter, K. M. 2021, *MNRAS*, 507, 3593
- 1483 Mor, R., Robin, A. C., Figueras, F., Roca-Fàbregas, S., & Luri, X. 2019, *A&A*, 624, L1
- 1484
- 1485 Morton, T. D., Bryson, S. T., Coughlin, J. L., et al. 2016, *ApJ*, 822, 86
- 1486
- 1487 Nardiello, D., Malavolta, L., Desidera, S., et al. 2022, *A&A*, 664, A163
- 1488
- 1489 Newton, E. R., Irwin, J., Charbonneau, D., et al. 2016, *ApJ*, 821, 93
- 1490 Newton, E. R., Mann, A. W., Kraus, A. L., et al. 2021, *AJ*, 161, 65
- 1491 Nordström, B., Mayor, M., Andersen, J., et al. 2004, *A&A*, 418, 989
- 1492
- 1493 Noyes, R. W., Hartmann, L. W., Baliunas, S. L., Duncan, D. K., & Vaughan, A. H. 1984, *ApJ*, 279, 763
- 1494
- 1495 O'Donovan, F. T., Charbonneau, D., Mandushev, G., et al. 2006, *ApJL*, 651, L61
- 1496
- 1497 Owen, J. E. 2019, *Annual Review of Earth and Planetary Sciences*, 47, 67
- 1498
- 1499 Owen, J. E., & Lai, D. 2018, *MNRAS*, 479, 5012
- 1500 Pecaut, M. J., & Mamajek, E. E. 2013, *ApJS*, 208, 9
- 1501 Petigura, E. A., Howard, A. W., Marcy, G. W., et al. 2017, *AJ*, 154, 107
- 1502
- 1503 Petigura, E. A., Marcy, G. W., Winn, J. N., et al. 2018, *AJ*, 155, 89
- 1504 Petigura, E. A., Rogers, J. G., Isaacson, H., et al. 2022, *AJ*, 163, 179
- 1505
- 1506 Plavchan, P., Barclay, T., Gagné, J., et al. 2020, *Nature*, 582, 497
- 1507 Price-Whelan, A. M., Sipőcz, B. M., Günther, H. M., et al. 2018, *AJ*, 156, 123
- 1508
- 1509 Quinn, S. N., White, R. J., Latham, D. W., et al. 2012, *ApJL*, 756, L33
- 1510
- 1511 Raghavan, D., McAlister, H. A., Henry, T. J., et al. 2010, *ApJS*, 190, 1
- 1512
- 1513 Rampalli, R., Agüeros, M. A., Curtis, J. L., et al. 2021, *ApJ*, 921, 167
- 1514
- 1515 Rana, N. C. 1991, *ARA&A*, 29, 129
- 1516 Rauer, H., Catala, C., Aerts, C., et al. 2014, *Experimental Astronomy*, 38, 249
- 1517
- 1518 Raymond, S. N., Kokubo, E., Morbidelli, A., Morishima, R., & Walsh, K. J. 2014, in *Protostars and Planets VI*, ed. H. Beuther, R. S. Klessen, C. P. Dullemond, & T. Henning, 595–618
- 1519
- 1520 Rebull, L. M., Stauffer, J. R., Hillenbrand, L. A., et al. 2022, *AJ*, 164, 80
- 1521
- 1522 Rebull, L. M., Stauffer, J. R., Bouvier, J., et al. 2016, *AJ*, 152, 114
- 1523
- 1524 Reinhold, T., Bell, K. J., Kuszlewicz, J., Hekker, S., & Shapiro, A. I. 2019, *A&A*, 621, A21
- 1525
- 1526 Reinhold, T., & Gizon, L. 2015, *A&A*, 583, A65
- 1527 Reinhold, T., Shapiro, A. I., Solanki, S. K., & Basri, G. 2023, *A&A*, 678, A24
- 1528
- 1529 Ricker, G. R., Winn, J. N., Vanderspek, R., et al. 2015, *Journal of Astronomical Telescopes, Instruments, and Systems*, 1, 014003
- 1530
- 1531 Rizzuto, A. C., Newton, E. R., Mann, A. W., et al. 2020, *AJ*, 160, 33
- 1532
- 1533 Rogers, J. G., & Owen, J. E. 2021, *MNRAS*, 503, 1526
- 1534 Ruiz-Lara, T., Gallart, C., Bernard, E. J., & Cassisi, S. 2020, *Nature Astronomy*, 4, 965
- 1535
- 1536 Sandoval, A., Contardo, G., & David, T. J. 2021, *ApJ*, 911, 117
- 1537 Santos, A. R. G., Breton, S. N., Mathur, S., & García, R. A. 2021, *ApJS*, 255, 17
- 1538
- 1539 Santos, A. R. G., García, R. A., Mathur, S., et al. 2019, *ApJS*, 244, 21
- 1540
- 1541 Saunders, N., van Saders, J. L., Lytle, A. J., et al. 2024, *ApJ*, 962, 138
- 1542
- 1543 Schmidt, S. P., Schlaufman, K. C., & Hamer, J. H. 2024, *AJ*, 168, 109
- 1544
- 1545 See, V., Yuxi, Lu, Amard, L., & Roquette, J. 2024, arXiv e-prints, arXiv:2405.00779
- 1546
- 1547 Sestito, P., & Randich, S. 2005, *A&A*, 442, 615
- 1548 Silva Aguirre, V., Bojsen-Hansen, M., Slumstrup, D., et al. 2018, *MNRAS*, 475, 5487
- 1549
- 1550 Simonian, G. V. A., Pinsonneault, M. H., & Terndrup, D. M. 2019, *ApJ*, 871, 174
- 1551
- 1552 Skrutskie, M. F., Cutri, R. M., Stiening, R., et al. 2006, *AJ*, 131, 1163
- 1553
- 1554 Skumanich, A. 1972, *ApJ*, 171, 565
- 1555 Snodgrass, H. B., & Ulrich, R. K. 1990, *ApJ*, 351, 309
- 1556 Soderblom, D. R. 2010, *ARA&A*, 48, 581
- 1557 Southworth, J. 2011, *MNRAS*, 417, 2166
- 1558 Sozzetti, A., Torres, G., Charbonneau, D., et al. 2007, *ApJ*, 664, 1190
- 1559
- 1560 Spada, F., & LanzaFame, A. C. 2020, *A&A*, 636, A76
- 1561 Thompson, S. E., Coughlin, J. L., Hoffman, K., et al. 2018, *ApJS*, 235, 38
- 1562
- 1563 Tofflemire, B. M., Rizzuto, A. C., Newton, E. R., et al. 2021, *AJ*, 161, 171
- 1564
- 1565 Tran, Q. H., Bowler, B. P., Cochran, W. D., et al. 2024, *AJ*, 167, 193
- 1566
- 1567 Vach, S., Zhou, G., Huang, C. X., et al. 2024, arXiv e-prints, arXiv:2403.03261
- 1568
- 1569 Van Der Walt, S., Colbert, S. C., & Varoquaux, G. 2011, *Computing in Science & Engineering*, 13, 22
- 1570
- 1571 Van Eylen, V., Agentoft, C., Lundkvist, M. S., et al. 2018, *MNRAS*, 479, 4786
- 1572
- 1573 van Saders, J. L., Ceillier, T., Metcalfe, T. S., et al. 2016, *Nature*, 529, 181
- 1574

- 1575 Vidotto, A. A., Gregory, S. G., Jardine, M., et al. 2014, MNRAS,
1576 441, 2361
- 1577 Villumsen, J. V. 1983, ApJ, 274, 632
- 1578 Virtanen, P., Gommers, R., Oliphant, T. E., et al. 2020, Nature
1579 Methods, 17, 261
- 1580 Vogt, S. S., Allen, S. L., Bigelow, B. C., et al. 1994a, SPIE
1581 Conference Series, ed. D. L. Crawford & E. R. Craine, Vol. 2198
- 1582 Vogt, S. S., Allen, S. L., Bigelow, B. C., et al. 1994b, in Society of
1583 Photo-Optical Instrumentation Engineers (SPIE) Conference
1584 Series, Vol. 2198, Society of Photo-Optical Instrumentation
1585 Engineers (SPIE) Conference Series, ed. D. L. Crawford & E. R.
1586 Craine, 362
- 1587 Walkowicz, L. M., & Basri, G. S. 2013, MNRAS, 436, 1883
- 1588 Wilson, R. F., Barclay, T., Powell, B. P., et al. 2023, ApJS, 269, 5
- 1589 Winn, J. N., Johnson, J. A., Narita, N., et al. 2008, ApJ, 682, 1283
- 1590 Wood, M. L., Mann, A. W., Barber, M. G., et al. 2023, AJ, 165, 85
- 1591 Xiang, M., & Rix, H.-W. 2022, Nature, 603, 599
- 1592 York, D. G., Adelman, J., Anderson, John E., J., et al. 2000, AJ,
1593 120, 1579
- 1594 Zakhzhay, O. V., Launhardt, R., Trifonov, T., et al. 2022, A&A,
1595 667, L14
- 1596 Zari, E., Hashemi, H., Brown, A. G. A., Jardine, K., & de Zeeuw,
1597 P. T. 2018, A&A, 620, A172
- 1598 Zhou, G., Wirth, C. P., Huang, C. X., et al. 2022, AJ, 163, 289
- 1599 Ziegler, C., Law, N. M., Morton, T., et al. 2017, AJ, 153, 66
- 1600 Zong, W., Fu, J.-N., De Cat, P., et al. 2018, ApJS, 238, 30

1601

APPENDIX

1602

A. ROTATION PERIOD CATALOG COMPARISON

1603 While we opted for the S19 and S21 rotation period catalogs, the (Deleted: recent) analysis by Reinhold et al. (2023) bears
 1604 comment. Reinhold et al. (2023) used a similar selection function as Santos et al. (all Kepler stars), and considered a novel period
 1605 measurement approach based on the gradient of the power spectrum (GPS). Their method likely provides greater completeness,
 1606 due to its greater sensitivity to signals that are only weakly periodic.

1607 Figure 10 shows histograms of the differences between reported periods from these various studies. The left panel compares
 1608 overlapping stars from McQuillan et al. (2014) and the Santos et al. studies. The periods agree at a precision of $\lesssim 0.01 P_{\text{rot}}$ for
 1609 $P_{\text{rot}} \lesssim 15$ days, and at $\lesssim 0.03 P_{\text{rot}}$ for $P_{\text{rot}} \approx 30$ days. A small bias exists at $P_{\text{rot}} \approx 10$ days, in the sense that the Santos periods tend to
 1610 be $\approx 1\%$ faster for such stars.

1611 The right panel compares overlapping periods from the Reinhold et al. (2023) GPS method and the Santos et al. studies. The
 1612 periods agree at a precision of $\lesssim 0.20 P_{\text{rot}}$ for $P_{\text{rot}} \lesssim 15$ days, and at $\lesssim 0.30 P_{\text{rot}}$ for $P_{\text{rot}} \approx 30$ days. A bias develops past $P_{\text{rot}} \gtrsim 30$ days,
 1613 in the sense that the Santos et al. periods tend to be 10-20% longer than the GPS periods. The origin of this larger scatter could
 1614 be connected to the need for the GPS method to determine the “ α calibration factor”, which is known only at a statistical level
 1615 for large stellar populations (see Reinhold et al. 2023). While we considered deriving independent rotation-based ages using the
 1616 Reinhold et al. (2023) GPS periods with an inflated empirical uncertainty, we ultimately opted against this path. A rotation period
 1617 difference of 20-30% away from the “true period” could sufficiently skew a star’s age that we prefer to restrict our attention to
 1618 the stars for which precision is a possible outcome.

1619 B. DEFINING AN “ISOCHRONALLY FAR FROM THE MAIN SEQUENCE” BOUNDARY

1620 The (arbitrary) method used to construct the orange line in the lower panel of Figure 1 was as follows. The line is defined as
 1621 the maximum of two numerically-determined functions, $f_0(T_{\text{eff}})$ and $f_1(T_{\text{eff}})$. We defined f_0 by fitting an N^{th} -order polynomial to
 1622 the stars with rotation periods for which $t_{\text{B20,iso}}/(+ \sigma_{t,\text{B20,iso}}) \approx 3$ and $T_{\text{eff}} \in [3700, 5900]$ K, where $t_{\text{B20,iso}}$ was the isochronal age
 1623 reported by Berger et al. (2020b). We let the order of the fit vary from $N=1$ to 10, minimized the Bayesian Information Criterion,
 1624 and found $N=6$. By eye, this yielded a plausible locus for $T_{\text{eff}} \lesssim 5300$ K. However, for F and G dwarfs, the resulting locus allowed
 1625 for stars that were “too evolved”; the density of KOIs was anomalously low in this region of the $\log g$ vs. T_{eff} plane. We therefore
 1626 visually selected KOIs that appeared to be near the main sequence – i.e. most of the yellow points in Figure 1 – and used them to
 1627 fit a separate polynomial f_1 through a similar BIC-minimization procedure, which yielded $N=3$. This polynomial, f_1 , is shown
 1628 in very faint opacity in Figure 1. The portion of the orange locus from ≈ 5300 – 6200 K is set as $f_1 + c$, for c a constant offset
 1629 that we defined to be 0.1 dex above the “KOI main sequence”. The exact break-point in temperature is automatically set by

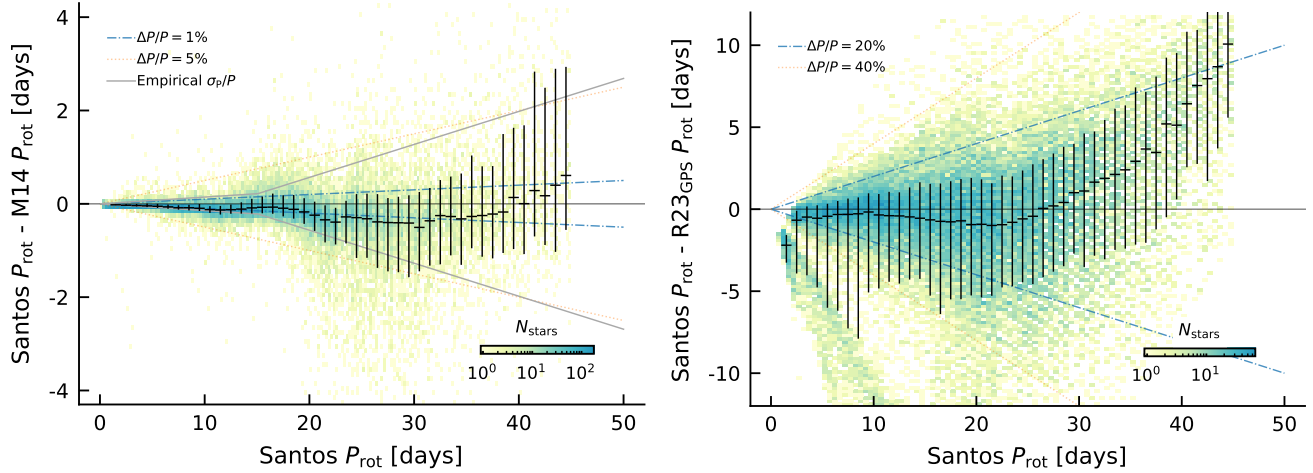


Figure 10. Comparison of reported literature stellar rotation periods. “Santos” refers to the concatenation of Santos et al. (2019) and Santos et al. (2021). “M14” refers to McQuillan et al. (2014). “R23_{GPS}” refers to the Gradient of Power Spectrum periods from Reinhold et al. (2023). The background is a 2-D histogram with a logarithmic color stretch that counts overlapping stars between these studies. The black errorbars show the median and $\pm 1\sigma$ range of period the differences in 1-day bins. The solid gray “empirical σ_P/P ” line in the left panel shows the expected $\pm 1\sigma$ range that would be spanned if the independent P_{rot} measurements had gaussian uncertainties drawn following the empirical estimate described in Section 2.1. Note the different vertical scales.

1630 max($f_0, f_1 + c$). While we do report rotation-based ages for stars above this orange locus, they are flagged as not being near the
 1631 main sequence in the log g vs. T_{eff} plane.

1632 C. CASES WITH “INCONSISTENT” ROTATION AND LITHIUM-BASED AGES

1633 In this section we discuss the systems with confirmed planets that have nominally discrepant rotation and lithium-based ages.
 1634 We find that only one of them, Kepler-786, is interesting.

1635 *Kepler-1* ——TrES-2/Kepler-1 (O’Donovan et al. 2006) is a \approx 2.5 day near-grazing hot Jupiter orbiting a G0 V primary which has
 1636 been studied in detail by multiple investigators (e.g. Sozzetti et al. 2007; Winn et al. 2008; Kipping & Bakos 2011; Southworth
 1637 2011). Our lithium-based age of this system (785^{+845}_{-419} Myr), derived from $\text{EW}_{\text{Li}}^* = 81 \pm 3$ mÅ, qualitatively agrees with the previ-
 1638 ously noted lithium abundance (Sozzetti et al. 2007). However, we detect no photometric rotation signal, and the spectroscopic
 1639 $v \sin i$ is low. The lithium age is strongly asymmetric because of the scatter in EW_{Li} vs. T_{eff} over ages $t \gtrsim 1$ Gyr for early G dwarfs.
 1640 We calculate a 2σ upper limit on t_{Li} of 2.8 Gyr, and a 3σ upper limit of 6.1 Gyr. The non-detection of rotation, while mildly
 1641 surprising, is not shocking if the system’s true age is in this long tail.

1642 *Kepler-101* ——This \approx 5500 K star has $\text{EW}_{\text{Li}}^* = 100 \pm 5$ mÅ, nominally implying $t_{\text{Li}} \approx 200$ -800 Myr, but no rotation detection. Our
 1643 automated flags noted that this star has a low surface gravity, high luminosity, and is far from the main sequence. Bonomo et al.
 1644 (2014) concur: this star is a sub-giant slightly more massive than the Sun; no rotation detection is expected; the lithium likely
 1645 simply survived over the star’s main sequence lifetime.

1646 *Kepler-108* ——This system of two mutually inclined giant planets (Mills & Fabrycky 2017) has a $T_{\text{eff}} \approx 5600$ K host star with
 1647 a strong lithium detection, and no rotation detection. The host star is entering the red giant branch; this has been previously
 1648 noted through asteroseismology (Huber et al. 2013), and our analysis of the Keck/HIRES spectrum with SpecMatch-Synth
 1649 (Petigura et al. 2017) concurs, yielding $T_{\text{eff}} = 5668 \pm 100$ K, $\log g = 3.8 \pm 0.1$, $[\text{Fe}/\text{H}] = 0.38 \pm 0.06$, and $v \sin i = 3.2 \pm 1.0$ km s $^{-1}$. Given
 1650 the star’s high mass, the high lithium content and lack of rotation detection is not surprising.

1651 *Kepler-786* ——This K3 V star has a surprisingly high lithium content. The spectrum is single-lined, with
 1652 SpecMatch-Synth derived parameters of $T_{\text{eff}} = 4769 \pm 100$ K, $\log g = 4.5 \pm 0.1$, $[\text{Fe}/\text{H}] = 0.11 \pm 0.06$, and $v \sin i = 2.4 \pm 0.6$ km s $^{-1}$.
 1653 Yet with $\text{EW}_{\text{Li}}^* = 83 \pm 6$ mÅ, the lithium age of 228^{+168}_{-87} Myr would predict (Replaced: an obvious replaced with: a short-period)
 1654 rotation signal. (Replaced: None is present in the Kepler light curve replaced with: The actual signal that is present has an
 1655 amplitude of ≈ 0.1 -0.3% and a period of ≈ 33 days), consistent with the low $v \sin i$. Out of all “apparently discrepant” lithium
 1656 and rotation measurements discussed in this appendix, this is the only one that seems to remain discrepant after scrutiny. The
 1657 Ca II doublet is in emission, with $R'_{\text{HK}} = -4.7 \pm 0.5$, which suggests an age at least as old as the Hyades (Mamajek & Hillenbrand
 1658 2008). The Balmer lines are in absorption, and display no obvious signatures of youth.

1659 *Kepler-1644* ——The rotation-based age of this system (77^{+144}_{-53} Myr) is nominally much lower than the lithium limit (> 767 Myr).
 1660 The Kepler light curve shows a $\approx 1\%$ amplitude 1.4 day rotation signal with many flares. However the automated quality flags note
 1661 that the star has low (photometric) surface gravity, a high RUWE ($\text{RUWE}_{\text{DR3}} = 7.0$), and that it is far from the main sequence. The
 1662 Keck/HIRES spectrum also shows visually narrow lines, with a SpecMatch-Synth $v \sin i \leq 2$ km s $^{-1}$. However, we performed
 1663 a cross-correlation between the HIRES spectrum and the nearest matches in the Keck/HIRES template library (Kolbl et al. 2015),
 1664 and found that on 31 July 2022 (UT) the system displayed a broad CCF with a blended second component at $\approx +26$ km s $^{-1}$
 1665 relative to the primary, with a best-fit flux-ratio of $\approx 3.4\%$, and a preferred $T_{\text{eff,B}} \approx 4400$ K. The spectrum and astrometric excess
 1666 noise therefore point to this system being an unresolved binary, which calls the reliability of the rotation-based age into question.
 1667 The non-detection of the companion from Robo-AO imaging at Palomar (Ziegler et al. 2017) suggests that the companion(s) are
 1668 likely within $\rho \lesssim 0.3''$.

1669 *Kepler-1699* ——This system is in a similar qualitative regime as Kepler-1644, with an apparently young $t_{\text{gyro}} = 85^{+106}_{-58}$ Myr derived
 1670 from a $\approx 2\%$ amplitude 4.2 day rotation signal, and no evidence for lithium. The system has $\text{RUWE}_{\text{DR3}} = 19.1$. From the same
 1671 style of CCF analysis from the Keck/HIRES spectrum acquired on 31 Aug 2022 (UT), we also find a double-peaked CCF, in this
 1672 case with a secondary component at ≈ -16 km s $^{-1}$ relative to the primary with $T_{\text{eff,B}} \approx 4900$ K. This putative companion is similarly
 1673 not detected in high-resolution imaging (Ziegler et al. 2017). The rotation-based age is questionable, given that we do not know
 1674 which source the rotation signal is from, or whether the stars have interacted.

1675 *Kepler-1943* ——This system nominally has a 409^{+520}_{-254} Myr lithium age, and no reported rotation detection. However, the star is
 1676 flagged as being over-luminous, low-surface gravity, and far from the main sequence. In other words, it is a subgiant.

1677 *Kepler-639, Kepler-320, Kepler-1719, Kepler-1876, Kepler-1072, Kepler-1743, Kepler-1929, Kepler-1488* ——These eight systems all
 1678 have nominally two-sided lithium age posteriors between 1 and 3 Gyr, and yet lack rotation period detections. All are subgiants,
 1679 flagged with Q_{star} under various combinations of bits 1, 2, and 9.

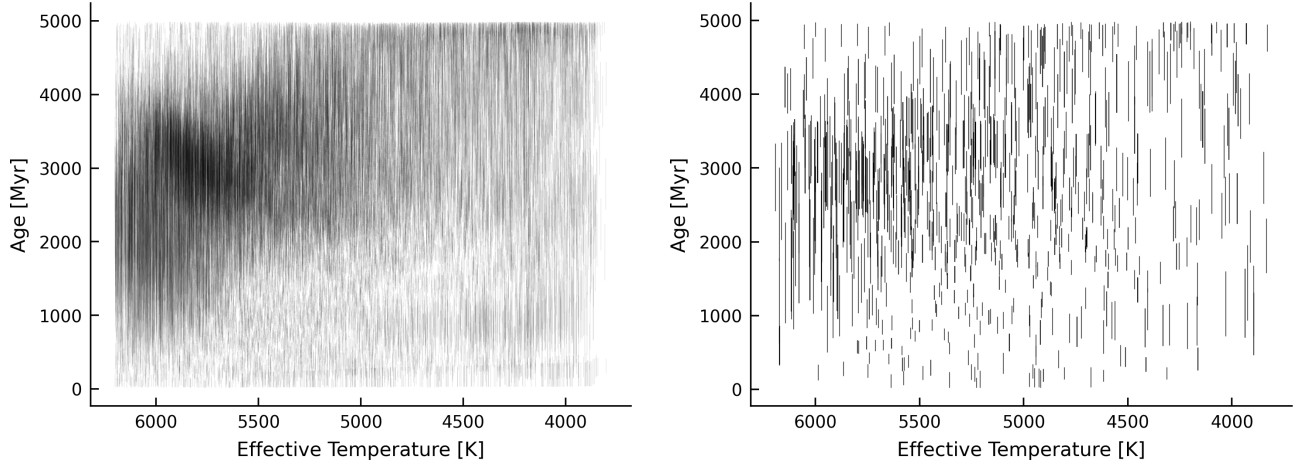


Figure 11. Rotation-based age vs. effective temperature. The entire Kepler sample is shown on the left. KOI hosts are shown on the right. Each bar shows the $\pm 1\sigma$ uncertainty for a star’s age as derived from its rotation period. Notable features are discussed in Appendix D.

D. AGE DIAGNOSTICS

1681 Figure 11 is a visualization of t_{gyro} vs. T_{eff} for our rotation-based age catalog. Each bar denotes the $\pm 1\sigma$ uncertainty for
 1682 a star’s rotation-based age: this plot can be viewed as the transformation of the left panel of Figure 2. The overdensity of
 1683 $P_{\text{rot}} \approx 20$ day G dwarfs corresponds to the large overdensity at $t_{\text{gyro}} \approx 3$ Gyr. The (non-physical) deficit of ~ 22 day rotators appears
 1684 as a deficit between 5500–6000 K. A second deficit is also visible from 3800–5000 K; it is associated with the “intermediate
 1685 period gap”, which may be associated with a transition from spot-dominated to faculae-dominated light curves (e.g. Reinhold
 1686 et al. 2019)(Added: , or with rapid spin-down at Rossby numbers near 0.5 (Lu et al. 2022)). At ≈ 1 Gyr, stalled spin-down
 1687 yields larger uncertainties for K dwarfs. The pile-up near ≈ 5 Gyr is imposed by our choice of prior; given that gyro-interp
 1688 returns non-calibrated ages in this regime, we truncated our analysis at 4 Gyr.

E. WHAT IF WE ONLY CONSIDERED MCQUILLAN’S PERIODS?

1689 We argued in Section 2.1 that adopting the periods from Santos et al. (2019, 2021) yielded the best possible balance between
 1690 homogeneity and sensitivity for both KOIs and for the broader Kepler sample. Nonetheless, it is interesting to consider what
 1691 would happen if we were to analyze only the rotation periods from McQuillan et al. (2014). Figures 12 and 13 repeat the
 1692 analysis, but make this alternate choice. Figure 12 shows that while the overall contours of the P_{rot} vs. T_{eff} distributions are
 1693 similar, the Santos et al. distribution includes more stars, particularly at longer rotation periods. This is connected to a stronger
 1694 noise-dependent cutoff in the McQuillan et al. (2014) sample than in the Santos et al. samples (see Masuda 2022b Figures 10
 1695 and 15). Figure 13 shows the impact on the inferred rotation-based age histograms: while the Santos et al. distribution peaks
 1696 at 2.8–3.0 Gyr, the McQuillan et al. distribution peaks at 2.4–2.6 Gyr. A number of metrics shift. For instance, the ratio of the
 1697 star formation rate 3 Gyr age to today is 2.81 ± 0.12 assuming the Santos et al. periods, and 2.24 ± 0.11 assuming the McQuillan
 1698 et al. periods. Similarly, the ratio of “old” (2–3 Gyr) to “young” (0–1 Gyr) stars shifts from 2.1 in the Santos et al. case to 1.9 in
 1699 the McQuillan et al. case. The K dwarf age distributions (Figure 13 lower panel) however appear quite similar. Generally, these
 1700 plots support the conclusion that the t_{gyro} age distribution in the Kepler field is non-uniform, with a peak in the (Replaced: 2.5
 1701 replaced with: 2.3)–3 Gyr range. Nonetheless, some of the details do shift depending on the choice of rotation detection pipeline.

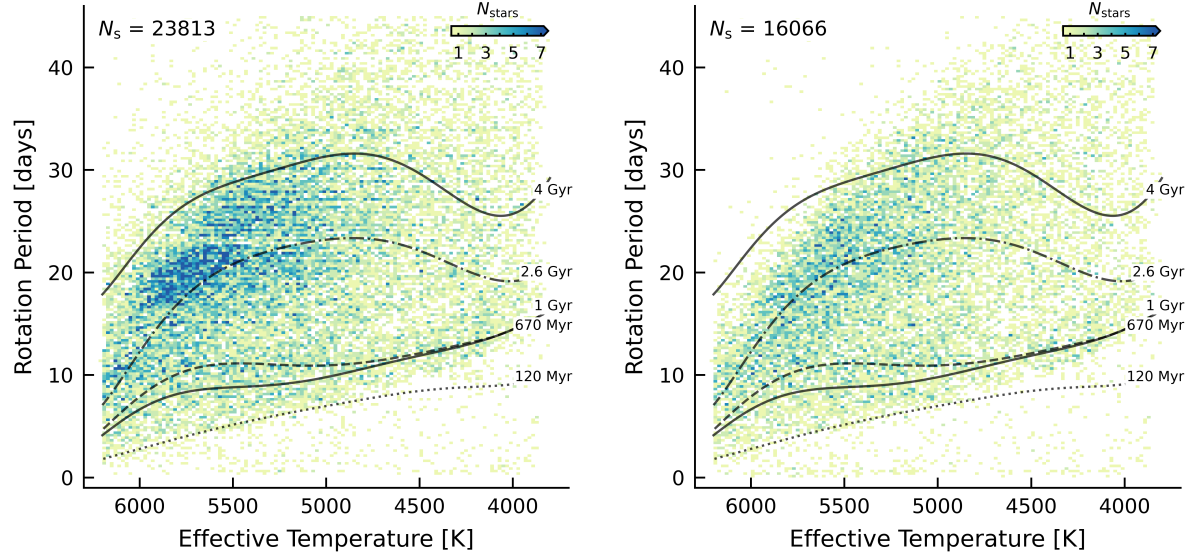


Figure 12. Variant of Figure 2, comparing the default rotation periods (*left*) from Santos et al. (2019, 2021) against the McQuillan et al. (2014) rotation periods (*right*). All stars are required to be amenable to rotation-based age dating (i.e. none of bit flags zero through (**Replaced:** nine replaced with: **ten**) raised).

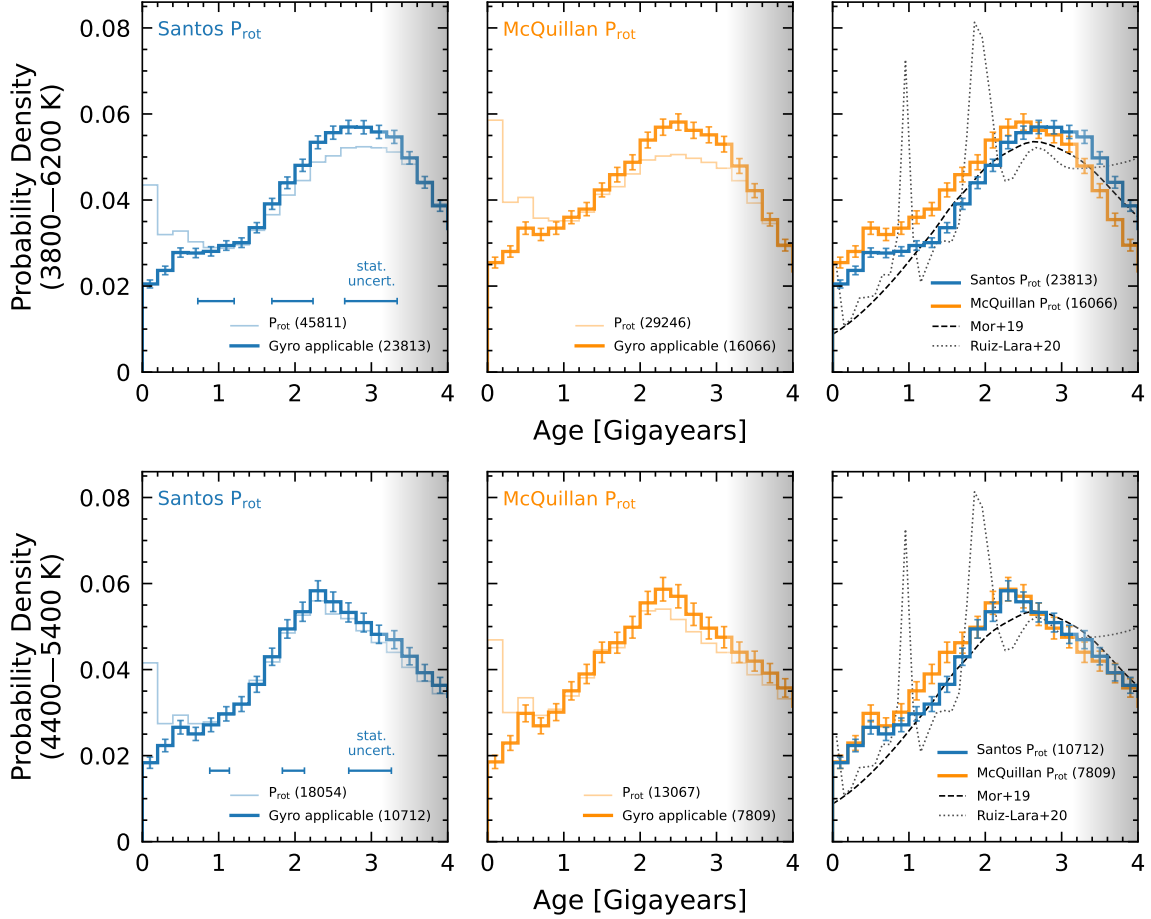


Figure 13. Variant of Figure 6, comparing our default adopted age distribution (left) based on the Santos et al. (2019, 2021) rotation periods against the age distribution (middle) based only on rotation periods reported by McQuillan et al. (2014).

List of Changes

Deleted: ~~accurately~~ on page 1.

Deleted: ~~We find that the scarcity of sub-gigayear systems can be attributed to the star formation rate in the Kepler field dropping by a factor of 2.81 ± 0.12 over the past 3 Gyr. We observe this trend both for known planet hosts and for the parent stellar sample. This “demographic cliff” in the Galaxy’s star formation history has been previously reported, and its confirmation helps clarify the age distribution of the known transiting exoplanets.~~ on page 1.

Added: The age distribution that we observe, rather than being uniform, shows that the youngest stars in the Kepler field are 3-5 times rarer than stars 3 Gyr old. This trend holds for both known planet hosts and for the parent stellar sample. We attribute the existence of this “demographic cliff” to a combination of kinematic heating and a declining star formation rate in the Galaxy’s thin disk, and highlight its impact on the age distribution of known transiting exoplanets. , on page 1.

Deleted: ~~a total of~~ on page 2, line 96.

Added: ~~than the 50 currently known~~, on page 2, line 98.

Replaced: ~~binary stars~~ replaced with: stars that are binaries and that have high metallicity, on page 2, line 150.

Deleted: ~~than in the past~~ on page 2, line 152.

Replaced: ~~the available single-star~~ replaced with: our, on page 2, line 159.

Replaced: ~~“mean-fits” to the rotation sequences of open clusters~~ replaced with: seventh-order polynomials fitted to the slow rotation sequences of open clusters (see Section 3.3 of Bouma et al. 2023), on page 4.

Deleted: ~~mean~~ on page 4.

Deleted: ~~and precise~~ on page 3, line 210.

Added: The gray lines in this figure are the polynomials described by Bouma et al. (2023) that fit the slow rotation sequences of the Pleiades (Rebull et al. 2016), Praesepe (Rampalli et al. 2021), NGC-6811 (Curtis et al. 2019), NGC-6819 (Meibom et al. 2015), Ruprecht-147 (Curtis et al. 2020), and M67 (Barnes et al. 2016; Dungee et al. 2022; Gruner et al. 2023),, on page 4, line 259.

Replaced: ~~these~~ replaced with: our adopted, on page 4, line 267.

Deleted: ~~adopted~~ on page 4, line 269.

Added: ~~v0 . 6;~~, on page 6, line 394.

Added: ~~in v0 . 6,~~ on page 6, line 413.

Deleted: ~~Kepler~~ on page 6, line 415.

Added: therefore, on page 6, line 417.

Added: Finally, we opted to modify gyro-interp in v0 . 6 to incorporate an age-dependent population-level Gaussian scatter, as detailed in the change log at [gyro-interp.readthedocs.io](https://github.com/keplergit/gyro-interp.readthedocs.io). While age precisions at ≤ 1 Gyr are unaffected, this update accounts for the observed intrinsic scatter in Ruprecht-147 and M67 being larger than in Praesepe or NGC-6811, potentially due to differential rotation (e.g., Epstein & Pinsonneault 2014). For $\approx 2\text{-}4$ Gyr old stars with rotation periods measured at $\approx 5\%$ precision, this change yields a $\lesssim 50\%$ increase in age uncertainties., on page 6, line 418.

Replaced: ~~nine~~ replaced with: ten, on page 6, line 445.

Replaced: ~~11~~ replaced with: 12, on page 6, line 448.

Added: We also considered a deeper cut ($\Delta G < 5$), and found it had negligible impact on our conclusions., on page 7, line 517.

Replaced: ~~HR~~ replaced with: HR or Kiel, on page 7, line 531.

Added: s, on page 7, line 532.

Added: Metallicity (bit 10)—Theoretical models suggest that stars with non-solar metallicities spin down at different rates than solar-metallicity stars (Amard & Matt 2020). This expectation has been hard to verify due to a dearth of nearby non-solar metallicity open clusters. However, if true, this effect could cause systematic biases for gyrochronone ages (e.g. Figure 9 of Clayton et al. 2020). We therefore flagged stars with spectroscopic $|[\text{Fe}/\text{H}]| > 0.3$ from either LAMOST DR5 (Zong et al. 2018) or CKS (Petigura et al. 2022) as being outside the range of our gyrochronology calibration. We discuss limitations of this approach in Section 8. , on page 8, line 540.

Replaced: ~~10~~ replaced with: 11, on page 8, line 552.

Replaced: 11 replaced with: 12, on page 8, line 562.

Added: , and for this plot, no attempt was made to exclude known binaries, on page 9.

Replaced: all stars with temperatures of 3800–6200 K for which we calculated rotational ages replaced with: stars with temperatures of 3800–6200 K, on page 10.

Added: metallicity, , on page 10.

Added: (see Section 4.1), on page 10.

Replaced: have more precise ages due to their fast spin-down replaced with: have more precise ages, on page 10.

Added: , and decreases rapidly at older ages, on page 10.

Replaced: assume Poisson statistics replaced with: are Poissonian, on page 10, line 690.

Replaced: yields replaced with: shows, on page 10, line 693.

Replaced: seems to replaced with: might, on page 11, line 710.

Added: Completeness—Figure 6 has a gray overlay beyond $\gtrsim 3$ Gyr because Kepler’s sensitivity to rotation signals diminishes at old ages., on page 11, line 734.

Deleted: this issue on page 11, line 737.

Added: Kepler’s completeness to rotation signals using MIIST-derived isochrone ages, on page 11, line 737.

Added: that are , on page 11, line 740.

Deleted: by Kepler on page 11, line 740.

Deleted: This trend is opposite in functional form to our derived age distributions. on page 11, line 742.

Added: This estimate suggests that while aspects of Figure 6 might be interpretable in terms of the Galaxy’s star formation history at $\lesssim 3$ Gyr, at older ages incompleteness precludes any such interpretation., on page 11, line 743.

Added: Temperature sensitivity—There are quantitative differences in Figure 6 between the K dwarfs (4400–5400 K) and the FGK stars (3800–6200 K). For instance, the distribution peaks at 2.3 Gyr for K dwarfs, and at 2.9 Gyr for the FGK sample. The peak is also sharper for the K dwarfs; its decrease from 2.3–3 Gyr is in an age range in which we believe the rotation period catalog completeness to be near unity. We show further details of the $t_{\text{gyro}} - T_{\text{eff}}$ distributions in Appendix D, and propose possible explanations for these differences in Section 8.2. , on page 11, line 748.

Deleted: Sub-gigayear planets can be particularly informative for studies of planet evolution. on page 11, line 760.

Added: This analysis provides an important path toward expanding the population of young and evolving exoplanets., on page 11, line 761.

Replaced: Star symbols denote 46 planets that are characterized in this work to have $t_{\text{gyro}} < 1$ Gyr at 2σ ; circles are planets from the literature meeting the same age requirement, but with a heterogeneous set of age provenances. Gray points are transiting planets from the NASA Exoplanet Archive older than 1 Gyr. If one were to instead select for precise ages ($t/\sigma_t > 3$), this would hide \approx ten < 0.5 Gyr planets, and add \approx fifteen 0.5–1 Gyr planets. For this plot, we require our Kepler stellar hosts to not have Q_{star} bits 0–9 raised, and for the planets to similarly not have quality flags raised. replaced with: Systems are selected to have $t < 1$ Gyr at 2σ . Star symbols denote 46 planets characterized in this work to have such ages at the highest confidence, meaning that none of Q_{star} bits 0–10 are raised, and the planets have no quality flags raised. Transparent crosses denote 17 planets for which either the planet is grazing, or the star has $\text{RUWE} > 1.4$. Gray points are from the NASA Exoplanet Archive. , on page 12.

Replaced: nine replaced with: ten, on page 12, line 849.

Replaced: This replaced with: The stars in this, on page 12, line 856.

Deleted: s on page 12, line 857.

Added: Two separate astrophysical effects might explain our observed age distribution (Figure 6): a declining star formation rate (SFR), and kinematic heating. Kinematic heating is associated with an increase in both stellar velocity dispersions and the disk’s vertical scale height over time (e.g. Villumsen 1983; Schmidt et al. 2024). The Kepler field points toward $(l, b) = (76.3^\circ, 13.5^\circ)$. A typical Kepler star at 1 kpc is therefore ≈ 230 pc above the galactic plane, a significant fraction of the thin disk’s mass-weighted ≈ 300 pc scale height (Bland-Hawthorn & Gerhard 2016). , on page 12, line 884.

Added: We assessed the relative importance of these two effects using the TRILEGAL Monte Carlo population synthesis tool , on page 13, line 895.

Added: TRILEGAL treats the Galaxy as a linear combination of a thin disk, thick disk, halo, and bulge, and allows for two possible SFRs: constant, and a “two-step” SFR in which the thin disk SFR is 50% larger from 1–4 Gyr than at other

ages. This two-step SFR was introduced to improve the model's ability to match star counts from Hipparcos and 2MASS , on page 13, line 897.

Added: For kinematic heating, TRILEGAL assumes that the disk scale height grows as $h_z = z_0(1+t/t_0)^\alpha$, for $\alpha=5/3$, $z_0=94.7$ pc, and $t_0=5.55$ Gyr, similar to Rana (1991). We queried the web interface toward the Kepler field, and toward the galactic plane (at $b=76.3^\circ$) to negate the effects of kinematic heating. We limited the output to stars with apparent Kepler magnitudes brighter than 16, and set the field of view to 10 deg^2 , the maximum available through the web interface. , on page 13, line 905.

Added: Figure 8 compares the results against our observed age distribution. The middle panel shows that assuming a constant SFR, kinematic heating alone can yield a two-fold difference in the abundance of the youngest stars relative to those ≈ 3 Gyr old. The right-most panel shows that additionally including the time-variable SFR yields the best agreement with the slope of our observed age distribution. , on page 13, line 914.

Deleted: Most stars observed by Kepler are in the thin disk. This can be verified by following Gaia Collaboration et al. (2018), and labeling stars with 2D tangential velocities $v_T < 40 \text{ km s}^{-1}$ as thin disk members, and those with $60 < v_T < 150 \text{ km s}^{-1}$ as thick disk members. These criteria yield 95,694 thin and 54,039 thick disk stars observed by Kepler. The thin disk stars have a threefold larger detected rotation period fraction: 35,675 rotators are in the thin disk, while 7,312 are in the thick disk. Further imposing the quality flags discussed in Section 4.1 yields 17,755 thin disk stars for which gyrochronology is applicable, and 2,462 thick disk stars. on page 13, line 922.

Deleted: Classifying Kepler stars as thin-vs. thick-disk members helps connect them to previous work on the Galaxy's star formation history. On extragalactic scales, the star formation rate in spiral galaxies with mass similar to the Milky Way peaked ≈ 10 Gyr ago, and has since decreased by an order of magnitude. on page 13, line 935.

Added: Despite the expected differences between pencil-beam surveys and volume-complete samples, our observed age distribution qualitatively agrees with a number of previous studies., on page 13, line 940.

Replaced: In our own galaxy, previous studies have replaced with: Previous work has, on page 13, line 944.

Added: weak , on page 14, line 969.

Added: ≈ 1 Gyr and , on page 14, line 970.

Added: s, on page 14, line 970.

Deleted: The ≈ 1 Gyr spike however is not recovered. on page 14, line 971.

Replaced: those studies is their improved accuracy replaced with: these previous studies is their accuracy, on page 14, line 976.

Added: (see Figure 5), on page 14, line 978.

Deleted: stellar- on page 14, line 982.

Deleted: stellar- on page 14, line 983.

Added: Astrophysical factors include metallicity, latitudinal differential rotation, mergers, and tidal spin-up. Observational limitations include the difficulty of measuring small-amplitude, long-period signals that are only quasi-coherent due to the starspot lifetime approaching the stellar rotation period. There is also the issue that our age-dating approach is not calibrated beyond 4 Gyr. In the following, we attempt to quantify the importance of these effects in our analysis, ordered by what we perceive to be their descending importance., on page 14, line 984.

Added: Simonian et al. (2019) for instance found that 59% of Kepler stars with rotation periods between 1.5 and 7 days lie 0.3 mag above the main sequence, compared with 28% of their full rotation sample. We attempted to mitigate the effects of binarity with five distinct quality flags (Section 4.1). This attempt was at least somewhat effective, based on the peak near zero in the raw distributions of Figure 6 being flattened in the cleaned distributions. However, the completeness of our quality flags is hard to assess. One specific concern is that these flags might have minimal sensitivity to binaries with separations of $\approx 0.05\text{-}0.5$ AU, for all but the highest mass ratios. This inner limit is set by the onset of detectable ellipsoidal variations in Kirk et al. (2016); the outer limit is set by the typical orbital periods of astrometric binaries in Gaia DR3 , on page 14, line 996.

Added: If we were not at all sensitive to binaries with separations of 0.05-0.5 AU, then based on the binary fraction and separation distribution from Raghavan et al. (2010), as much as $\approx 5\%$ of our “gyro applicable” sample (1,190/23,813 stars) might be contaminated. In a worst case scenario, all of these unidentified binaries might induce $P_{\text{rot}} < 10$ days, which would then be mixed in with the bona fide young, single stars. This would constitute a major source of contamination, given that our nominal sample of apparently clean stars had 2,706 stars with $P_{\text{rot}} < 10$ days. , on page 14.

Added: Figure 9 shows the rotation-based age distribution calculated by randomly dropping 1,190 of the $P_{\text{rot}} < 10$ day stars. Relative to the nominal “gyro applicable” age distribution, there are three important differences. There is a much larger

drop in the star formation rate over the past three gigayears, by a factor of 4.81 ± 0.26 , rather than 2.81 ± 0.12 . The rate of decline in star formation since ≈ 2.8 Gyr ago is also constant, rather than having a “kink” at 1.5 Gyr. And finally, the corrected distributions show closer agreement with both the SFHs derived from CMD fitting, and also with the KOI host distribution, which is almost devoid of close binaries within 1 AU (e.g. Moe & Kratter 2021, and references therein). We caution however that this correction assumes that *none* of our quality flags were able to identify any of these unresolved binaries. Since we did in fact include flags based on e.g., location in the HR diagram, this correction is best interpreted as an upper limit on the possible impact of binarity., on page 14.

Added: *Rotational outliers:* , on page 14.

Replaced: **young stars known to host planets** replaced with: **each star in our sample**, on page 14.

Deleted: **open**- on page 14.

Deleted: **open**- on page 14.

Added: While most of these outliers are known to have bad quality flags, some do not., on page 14.

Added: A separate plausible origin for rotational outliers is that they come from erroneously reported rotation periods. While the large surveys do show good internal consistency (Appendix E), the referee correctly pointed out that this is only a comparative test of methods, rather than an ability to recover ground truth (e.g. Aigrain et al. 2015). One could imagine an adversarial scenario in which, say, 10-20% of stars with $P_{\text{rot}} > 20$ days are erroneously reported, and in fact have much longer rotation periods. In this scenario, a similar analysis to that in Figure 9 showed that our analysis would overestimate the degree by which the SFR in the Kepler field has decreased, by 7-14%. , on page 15.

Added: Other age indicators may help in verifying the ages of the $\lesssim 3$ Gyr stars that are the main focus of this work. Specifically, chromospheric emission in the X-ray, Ca II HK line, and the UV can serve as an age tracer (Mamajek & Hillenbrand 2008; Vidotto et al. 2014; Engle 2024). However, these age indicators are all in a sense “rotation-powered”. The dynamo converts kinetic energy into magnetic energy, which is emitted through these chromospheric pathways. We did not attempt to incorporate these indicators into this study due to concerns regarding sensitivity, homogeneity, and the question of whether they in fact provide age information that is truly independent from rotation., on page 15.

Added: *Weakened magnetic braking:* If we lived in a universe in which stellar rotation rates and spot-induced photometric amplitudes remained *constant* after ≈ 3 Gyr, then older stars could contaminate the peaks in Figure 6. This scenario deserves consideration, given asteroseismic evidence for slowed spin-down rates after ≈ 4 Gyr for Sun-like stars (van Saders et al. 2016; Hall et al. 2021; Saunders et al. 2024), and the “long-period edge” in the $P_{\text{rot}} - T_{\text{eff}}$ distribution which may pile up over similar timescales (David et al. 2022). However, the stalling is thought to happen at > 5 Gyr for late-G dwarfs and early K dwarfs (e.g. Figure 4 by Saunders et al. 2024). This means that it cannot explain the 2.3 Gyr peak in the 4400-5400 K age distribution shown in Figure 6. Independently, the study by Masuda (2022a) fitted isochrones to a high-quality subset of Kepler data, and found that the McQuillan et al. (2014) sample, discussed in Appendix E, does not include many stars older than ≈ 4 Gyr. These arguments suggest that the peak in the age distribution is not caused by a pile-up of much older stars with lethargic spin-down rates, but that it could be contaminated by them beyond ≈ 3 Gyr, especially for stars hotter than the Sun. , on page 15.

Added: *Metallicity:* Stars with higher metallicity are thought to have longer convective turnover times, which may slow their rate of spin-down (Amard & Matt 2020). While observational studies of this effect have been suggestive, further work remains to definitively establish the importance of the effect (e.g. Amard et al. 2020a; See et al. 2024) Nonetheless, based on the theoretical predictions, we flagged stars with known spectroscopic $|[\text{Fe}/\text{H}]| > 0.3$, based on either LAMOST or Keck/HIRES spectra (Zong et al. 2018; Petigura et al. 2022). The main limitation of this approach is that only 53.3% of the stars in Table 2 with $t_{\text{gyro}} < 4$ Gyr had such spectra available. For the rest of the sample, primarily composed of fainter stars, this means that our quality flags were not sensitive to metallicity outliers. Based on the metallicity distribution of stars for which we do have spectra, this implies that at most $\approx 5\%$ of stars in our sample might have $|[\text{Fe}/\text{H}]| > 0.3$, with a slight bias toward lower metallicity stars over higher metallicity. Based on the results by Claytor et al. (2020), this will be most important for stars near the Kraft break, which could have ages over-estimated by $\approx 50\text{-}100\%$ if they are in fact metal-poor, and under-estimated in the converse case. , on page 15.

Added: *Differential rotation:* The Sun’s surface rotates once per $\approx 25\text{-}30$ days at latitudes between the equator and $\approx \pm 60^\circ$ (Snodgrass & Ulrich 1990). This latitudinal surface differential rotation yields two separate limitations on rotational ages. The first is on the accuracy with which any one star’s rotation period can be measured over a few-year mission like Kepler; the second is on the degree to which the intrinsic scatter in open cluster rotation sequences can be measured (e.g. Epstein & Pinsonneault 2014). In this study, we accounted for the latter intrinsic scatter based on available measurements from Ruprecht-147 (Curtis et al. 2020) and M67 data (Barnes et al. 2016; Dungee et al. 2022; Gruner et al. 2023). This means that irrespective of the assumed P_{rot} measurement precision, our model imposed a $\approx 5\text{-}10\%$ level of intrinsic P_{rot} scatter (perhaps differential-rotation induced) at old ages. While this accounts for the statistical impact of differential rotation

on the inferred age distribution, the accuracy issue remains; any one individual star's observed rotation period might be faster or slower than average stars of the same mass and age. This effect can yield a $\approx 20\%$ age bias for individual Sun-like stars with ages of a few billion years; the statistical uncertainties in Table 2 should be treated with appropriate caution. , on page 16.

Deleted: Metalliecity may also be relevant (Amard et al. 2020b; See et al. 2024). An additional caveat is that our rotation-based ages used photometric effective temperatures (Section 3), even though spectroscopic temperatures are available for the planet-hosting subset. This decision was driven by a desire for homogeneity irrespective of planet-hosting status. However it implies that the estimated planet ages might shift if one were to account for the spectroscopic information. on page 16.

Deleted: Other age indicators may help in verifying the ages of the $\lesssim 3$ Gyr stars that are the main focus of this work. Specifically, chromospheric emission in the X-ray, Ca H HK line, and the UV can serve as an age tracer (Mamajek & Hillenbrand 2008; Vidotto et al. 2014; Engle 2024). However, these age indicators are all in a sense “rotation-powered”. The dynamo converts kinetic energy into magnetic energy, which is emitted through these chromospheric pathways. We did not attempt to incorporate these indicators into this study due to concerns regarding sensitivity, homogeneity, and the question of whether they in fact provide age information that is truly independent from rotation. on page 16.

Added: Ages of stars older than the Sun: , on page 16.

Deleted: A broader question, beyond the scope of this work, concerns the ages of stars $\gtrsim 4$ Gyr old. on page 16.

Added: This work was limited to stars younger than 4 Gyr, on page 16.

Added: Planet, on page 16.

Replaced: the youngest “field stars” replaced with: these young stars, on page 16.

Added: due to its astrophysical depletion rate, on page 17.

Replaced: resulting ages replaced with: results, on page 17.

Replaced: sub-gigayear-confirmed replaced with: such, on page 17.

Added: (e.g. Kepler-1312 c and Kepler-1561 b) , on page 17.

Deleted: new on page 17.

Added: at least , on page 17.

Deleted: The star formation rate today is 2.81 ± 0.12 times lower than it was three billion years ago. on page 17.

Added: The youngest stars in the Kepler field (0-0.3 Gyr) are at least 2.81 ± 0.12 times rarer than stars 3 Gyr old. The statistical uncertainty on this value is dwarfed by the systematic uncertainty in the contamination rate of unresolved photometric binaries, which could push it as high as 4.81 ± 0.26 (Section 8.2), on page 17.

Replaced: This result replaced with: This range of values, on page 17.

Replaced: from rotation-based ages broadly agrees replaced with: is broadly consistent, on page 17.

Replaced: recent reports of a declining star-formation rate replaced with: modeling expectations (Section 8.1), and with age distributions derived from, on page 17.

Replaced: , though with the replaced with: . The , on page 17.

Added: rotation-based ages however is their , on page 17.

Replaced: sensitivity replaced with: accuracy, on page 17.

Replaced: implies replaced with: suggests, on page 17.

Replaced: derived replaced with: reported, on page 17.

Deleted: recent- on page 24.

Replaced: an obvious replaced with: a short-period, on page 25.

Replaced: None is present in the Kepler light curve replaced with: The actual signal that is present has an amplitude of $\approx 0.1\text{--}0.3\%$ and a period of ≈ 33 days, on page 25.

Added: , or with rapid spin-down at Rossby numbers near 0.5 (Lu et al. 2022), on page 26.

Replaced: 2.5 replaced with: 2.3, on page 26.

Replaced: nine replaced with: ten, on page 27.